

1 Article

2 

# Satellite Retrieval of Downwelling Shortwave 3 Surface Flux and Diffuse Fraction under All Sky 4 Conditions in the Framework of the LSA SAF 5 Program (Part 2: Evaluation)

6 **Dominique Carrer<sup>1</sup>, Suman Moparthi<sup>1</sup>, Chloé Vincent<sup>1</sup>, Xavier Ceamanos<sup>1</sup>, Sandra C. Freitas<sup>2</sup> and  
7 Isabel F. Trigo<sup>2</sup>**8 <sup>1</sup> Météo-France/CNRM, CNRS/GAME, 42 avenue Gaspard Coriolis, 31057 Toulouse Cedex, France9 <sup>2</sup> Instituto Português do Mar e da Atmosfera (IPMA), Rua C-Aeroporto, 1749-077 Lisboa, Portugal10 **Abstract:** High frequency knowledge of the spatio-temporal distribution of the Downwelling  
11 Surface Shortwave Flux (DSSF) and its diffuse fraction (fd) at the surface is nowadays essential for  
12 understanding climate processes at the surface-atmosphere interface, plant photosynthesis and  
13 carbon cycle, and for the solar energy sector. The EUMETSAT Satellite Application Facility for Land  
14 Surface Analysis operationally delivers estimation of the MDSSFTD (Downwelling Surface Short-  
15 wave radiation Fluxes – Total and Diffuse fraction) product with an operational status since the year  
16 2019. The method for the retrieval was presented in the companion paper [40]. The part 2 now  
17 focuses on the evaluation of the MDSSFTD algorithm and presents the comparison of the  
18 corresponding outputs, i.e. total DSSF and diffuse fraction (fd) components, against *in-situ*  
19 measurements acquired at four BSRN stations over a seven-month period. The validation is  
20 performed on an instantaneous basis. We show that the satellite estimates of DSSF and fd meet the  
21 target requirements defined by the user community for all-sky (clear and cloudy) conditions. For  
22 DSSF, the requirements are  $20\text{Wm}^{-2}$  for  $\text{DSSF} < 200\text{Wm}^{-2}$ , and 10% for  $\text{DSSF} \geq 200\text{Wm}^{-2}$ . The MBE and  
23 rMBE compared to the ground measurements are  $3.618\text{Wm}^{-2}$  and 0.252%, respectively. For fd, the  
24 requirements are 0.1 for  $\text{fd} < 0.5$ , and 20% for  $\text{fd} \geq 0.5$ . The MBE and rMBE compared to the ground  
25 measurements are -0.044 and -17.699%, respectively. The study also provides a separate analysis of  
26 the product performances for clear sky and cloudy sky conditions. The importance of representing  
27 the cloud-aerosol radiative coupling in the MDSSFTD method is discussed. Finally, it is concluded  
28 that the quality of the Aerosol Optical Depth (AOD) forecasts currently available is enough accurate  
29 to obtain reliable diffuse solar flux estimates. This quality of AOD forecasts was still a limitation a  
30 few years ago.31 **Keywords:** Solar Radiation; Meteosat Second Generation; Validation; Land Surface Modelling

32

33 

## 1. Introduction

34 The downwelling surface short-wave radiation flux (DSSF) refers to the radiative energy in the  
35 wavelength interval  $[0.3\text{ }\mu\text{m}, 4.0\text{ }\mu\text{m}]$  reaching the Earth's surface per time and area unit. An accurate  
36 knowledge of the spatio-temporal distribution of the downwelling solar radiation at the surface is  
37 essential not only for understanding climate processes at the surface-atmosphere interface [1, 2], but  
38 also for plant photosynthesis and carbon cycle, e.g., [3-5] and for the solar energy sector [6].  
39 Concerning the current status of DSSF modelling in atmospheric models, [7] and [8] found that the  
40 National Centers for Atmospheric Prediction (*NCEP*) and the National Center for Atmospheric  
41 Research (*NCAR*) data consistently overestimated DSSF by 17%–27%. Comparisons with satellite data  
42 have also revealed large positive biases in *NCEP–NCAR* DSSF ranging from 25 to 50  $\text{Wm}^{-2}$  over the  
43 United States [9-10] and from 40 to 80  $\text{Wm}^{-2}$  over Europe [11]. However, in a recent study, [12]  
44 examined the progress made by two new reanalyses in the estimation of surface irradiance (ERA5

45 and COSMO-REA6) and negative biases of around  $-5 \text{ Wm}^{-2}$ . They showed the largest deviations  
46 under clear-sky conditions, which is most likely caused by the aerosol data used.

47 DSSF essentially depends on the solar zenith angle, cloud coverage, aerosols, and to a lesser  
48 extent on atmospheric absorption and surface albedo. Over the past few decades the scientific  
49 community has developed computation methods to estimate both downward and net surface solar  
50 irradiance from satellite observations [13-29]. In addition to those estimates, two incoming solar  
51 radiation products derived from MSG/SEVIRI were also developed, being operated since 2005 by  
52 EUMETSAT Satellite Application Facility (SAF) on Land Surface Analysis (LSA; [30]): the MDSSF  
53 product (referenced LSA-201) corresponding to instantaneous values, and the DIDSSF product (LSA-  
54 203) corresponding to daily accumulated values. Both products consider clear and cloudy skies to  
55 provide total shortwave fluxes at the surface. However, all these estimates lack of the repartition of  
56 the total flux into its direct and diffuse components (through the diffuse fraction, for example).  
57 Moreover, even though these products have proven to be of high quality, [31-33] showed that they  
58 still have some limitations under clear sky conditions, especially as they are determined taking as  
59 hypothesis a temporally and spatially constant load and type of continental aerosols [34]. The  
60 importance of aerosols on the DSSF has been established in numerous studies on some highly  
61 polluted regions [35-39]. Thus, an initiative has been conducted by EUMETSAT to upgrade the  
62 physics in the scientific algorithms used for the satellite-derived DSSF retrievals and to provide first  
63 estimations of the diffuse fraction of the radiation.

64 The physics of this upgraded algorithm is described in the companion paper [40]. The new  
65 product version has been referenced as LSA-207 by EUMETSAT, corresponding to the MSG  
66 Downwelling Surface Short-wave radiation Fluxes – Total and Diffuse fraction (MDSSFTD). Two  
67 different modules are used to calculate the set of MDSSFTD outputs, one for clear conditions, and the  
68 other for cloudy conditions. The two methods are designed to ensure the spatial and temporal  
69 continuity of DSSF and diffuse fraction in the LSA-207 product. Details on the methodology as well  
70 as the major limitations are given in [40]. The input cloud mask is used to distinguish between the  
71 two methods. The summary of the two methods is as follows and described in detailed in [40].

72 In clear sky conditions, the formulation based on the algorithm SIRAMix [41, 42] is used to  
73 estimate the total flux and the diffuse fraction. The atmospheric pressure, water content, ozone  
74 content, aerosols vary in time and space and are provided by atmospheric model forecasts. Both  
75 direct and diffuse flux terms are estimated by combining pre-computed aerosol transmittances and  
76 albedo (computed using radiative transfer models for varying aerosol load, solar zenith angles and  
77 water vapour content) from look-up tables and semi-empirical radiative transfer equations [42]. The  
78 total flux is the sum of both direct and diffuse flux estimates. The diffuse fraction is obtained as the  
79 ratio of the diffuse flux to the total flux estimate. In cloudy sky conditions, the total flux is estimated  
80 using simplified radiative transfer equations as described in [40]. The cloud transmittances are  
81 estimated from SEVIRI radiances at the top-of-atmosphere (TOA) level. The atmospheric  
82 transmittance term used for the estimation of the effective transmittance remains the same as in clear  
83 sky conditions. However, an extra cloud transmittance term is added as well as two multiple  
84 scattering terms. In the case of cloudy-sky conditions, the diffuse fraction is estimated using an  
85 empirical formulation. The clear-sky and cloudy sky methods are designed to provide smooth  
86 transitions in the frontiers between clear and cloudy pixels (see [40]). Finally, LSA-207 then includes  
87 an estimation of the total incoming solar radiation with an improved modelling of the aerosol impact  
88 on the atmospheric transmittance compared to the previous MDSSF product (LSA-201). The diffuse  
89 fraction of the radiation for all sky conditions is now also available. Moreover, estimations of  
90 auxiliary quantities are also provided: the equivalent Aerosol Optical Depth (AOD) at 550nm, the  
91 Opacity Index (OI) characterizing the opacity of the atmosphere (defined in [40]), and a quality flag  
92 information (QF).

93 This study makes an evaluation of the satellite-derived MDSSFTD product. The article is  
94 organized as follows. Section 0 presents the data and the metrics used for the validation. Section 0  
95 presents validation results and Section 0 concludes about the performance of the product regarding  
96 the users requirements.

97 **2. Data and Metrics**98 **2.1. Requirements**

99 Over India, a satellite-based surface solar radiation dataset called Surface Solar Radiation Data  
 100 Set-Heliosat (SARAH-E) was developed and evaluated against *in-situ* measurements over a variety  
 101 of sites. The results indicate an overestimation of the satellite DSSF, with a mean bias of  $21.9\text{Wm}^{-2}$   
 102 [43]. Study Over Finland and Sweden [44] also discussed the retrieval accuracies of two different  
 103 satellite-derived DSSF dataset (the polar-orbiting satellite-based dataset – CLARA-A1 – and the  
 104 geostationary satellite-based dataset – SARAH). They showed comparable accuracies in comparison  
 105 with ground measurements, in particular  $10\text{Wm}^{-2}$  for the monthly means metrics and  $15\text{Wm}^{-2}$  for  
 106 daily means metrics. Over Europe, [31] completed the inter-comparison of satellite-derived incoming  
 107 solar products from the different Satellite Application Facilities of EUMETSAT and concluded that  
 108 the products have comparable mean biases ( $+4\text{Wm}^{-2}$ ) and root mean square differences ( $80\text{-}100\text{Wm}^{-2}$ )  
 109 for instantaneous metrics. Performances of the historical LSA-SAF DSSF (LSA-201) satellite-derived  
 110 incoming solar radiation product were also discussed more in detail in [45,46]. On an instantaneous  
 111 basis, the bias between the satellite product and the ground data was shown to be small with absolute  
 112 values of less than  $10\text{ Wm}^{-2}$  over Europe [45], and even lower over France ( $3.75\text{Wm}^{-2}$  representing  
 113 2.5%). The standard deviation of the difference between instantaneous satellite estimates and ground  
 114 measurements were of the order of  $40\text{ Wm}^{-2}$  for clear sky data and  $110\text{Wm}^{-2}$  for cloudy sky data.  
 115 Finally, the satellite estimates of DSSF are today ranging in average from 10 to  $30\text{ Wm}^{-2}$  in absolute  
 116 bias scale. However, these past works also pointed out that the absolute metrics usually used to  
 117 evaluate the product performances are not equivalent if the domain (or period) of interest is located  
 118 in high latitude or in low latitudes (or winter and summer periods).

119 The characteristics of the LSA-207 MDSSFTD product and the targeted accuracies agreed with  
 120 EUMETSAT are described in Table 1. These are a compromise between what is currently achievable,  
 121 given existing observations and algorithm input data, and what would suit most users and applications.  
 122 In this respect, the ‘threshold’ requirement is then defined as the minimum accuracy which is  
 123 acceptable for DSSF user needs. This paper assesses the performance of the product by referring to  
 124 the ‘target’ requirement. However, it may be relevant to note that because the topic of retrieving  
 125 diffuse fraction from satellite is very recent, there is today no performance requirements defined by  
 126 the scientific community for this parameter. We therefore have fixed the ‘target’ accuracy to 20%,  
 127 although a larger uncertainty (e.g.  $>30\%$ ) could have been also considered. The target accuracy  
 128 metrics used are the Mean Bias Error (MBE) for low values, and the relative MBE (rMBE) for high  
 129 values of DSSF or fd.

130 **Table 1 Product Requirements for MDSSFTD, in terms of area coverage, resolution and accuracy.**  
 131 The targeted requirements are indicated in bold.

| Product                                                                      | Coverage | Resolution |                      |           | Accuracy                                                                                                                  |         |     |
|------------------------------------------------------------------------------|----------|------------|----------------------|-----------|---------------------------------------------------------------------------------------------------------------------------|---------|-----|
|                                                                              |          | Temporal   | Spatial              | Threshold | Target                                                                                                                    | Optimal |     |
| <b>MDSSFTD (LSA-207)</b><br><b>DSSF_TOT</b>                                  | MSG disk | 15 min     | MSG pixel resolution | 20%       | DSSF< $200\text{ Wm}^{-2}$ :<br><b>20W/m<sup>2</sup> (MBE)</b><br>DSSF $\geq$ $200\text{ Wm}^{-2}$ :<br><b>10% (rMBE)</b> |         | 5%  |
| <b>MDSSFTD (LSA-207)</b><br>Diffuse Fraction<br><b>FRACTION_DIFFUSE (fd)</b> | MSG disk | 15 min     | MSG pixel resolution | 30%       | <b>fd &lt;0.5: 0.1 (MBE)</b><br><b>fd <math>\geq</math>0.5: 20% (rMBE)</b>                                                |         | 10% |

132 **2.2. Ground measurements and preprocessing**

133 Four ground stations are used for the validation analyses presented in this document. The  
 134 stations considered are Carpentras, De Aar, Tamanrasset and Toravere from the BSRN (Baseline  
 135 Surface Radiation Network, <http://www.bsrn.awi.de>) of the World Climate Research Programme.  
 136 Their location is presented in Figure 1.

137 The *in-situ* measurements of instantaneous total and diffuse DSSF as observed at these stations  
 138 are used as reference. The stations are located in climatically different regions of Europe and Africa.  
 139 For example, the station Tamanrasset in North Africa is influenced by coarser dust particles and more  
 140 clear conditions than the other Europe-based stations. Toravere is located at the highest latitude and  
 141 therefore is related to frequent periods of overcast in the winter and fall. This will help evaluation the  
 142 MDSSFTD method under cloudy situation and high solar zenith angles.



**Figure 1** Location of the ground stations providing *in-situ* measurements.

143 BSRN derived surface flux values are retrieved at a high temporal frequency going from 1  
 144 minute to a few minutes. BSRN data already account for missing or bad measurements for which  
 145 missing flag values are assigned. The missing values are discarded in the comparison with satellite  
 146 flux measurements. The direct flux measurements account for the varying solar zenith angle  
 147 dependence. All measurements (total, diffuse and direct surface solar flux measurements) are  
 148 discarded when the solar zenith angle is greater than 80 degrees. MSG/SEVIRI satellite-derived  
 149 products differ on a pixel basis from 0 to 12 minutes with the product time. SEVIRI scan takes 12  
 150 minutes for the data acquisition over the MSG disk starting from the South pole and finishing its  
 151 acquisition in the North pole. For the sake of a fair comparison, the ground measurements are  
 152 averaged over 15 minutes, centered around the exact acquisition time of the satellite for every SEVIRI  
 153 pixel. The relationship between the estimated time difference as a function of row number (or latitude)  
 154 is detailed in other LSA SAF reports (product user manual MDSSF; 2.6V2 at  
 155 <https://landsaf.ipma.pt/en/products/longwave-shortwave-radiation/>; last time consulted on 2<sup>nd</sup> of  
 156 September, 2019). Note that the diffuse fraction is not a direct measurement. This variable is obtained  
 157 by dividing the diffuse component over the total component that are measured by the ground  
 158 instruments. The BSRN total fluxes and diffuse fluxes are measured respectively with pyranometers  
 159 and shaded pyranometers (Kipp & Zonen/CM21 for stations Carpentras and Toravere, Kipp &  
 160 Zonen/CMP21 for station De Aar, and Eppley/PSP for station Tamanrasset). The accuracy of the  
 161 BSRN total fluxes measurements, provided the measure is made according to the BSRN protocol, is  
 162 estimated to 0.5% or 1.5 W m<sup>-2</sup>, while the accuracy of the diffuse measurements is estimated to 2%  
 163 or 3 W m<sup>-2</sup> [47]. In practice, specific analyses on BSRN sites accuracy [48-49] confirmed that the  
 164 uncertainty of the measures are in agreement with such levels of uncertainties, with some limitations  
 165 for low sun elevation angles and low radiation fluxes. As the validity of the MDSSFTD products are  
 166 limited to sun zenith angles below 80°, we consider that the in situ measurement of total fluxes and  
 167 the BSRN-derived diffuse fractions can reasonably be taken as references for our validation analysis.

168 2.3 CAMS all-sky radiation data

169 The Copernicus Atmosphere Monitoring Service (CAMS) all-sky radiation data was also used  
 170 to compare with the MDSSFTD product. CAMS all-sky radiation service distributes global, direct and  
 171 diffuse irradiances as well as a direct at normal incidence irradiance, for all-sky (clear+cloud), clear-  
 172 sky only, and cloudy-sky only. These data are provided as timeseries with a temporal resolution of  
 173 1-minute, 15-minutes, 1h, 1 day or 1 month, and are made available since February 2004 with a 2-  
 174 days delay. The spatial coverage corresponds to the Meteosat Second Generation (MSG) disk. To  
 175 produce the timeseries, radiation data is spatially interpolated to the point of interest from a product  
 176 available at the native spatial resolution of MSG/SEVIRI. These data are publicly available from the  
 177 CAMS portal (<https://atmosphere.copernicus.eu/solar-radiation>, last consulted on 18/10/2019).

178 The CAMS Radiation service relies on the Heliosat-4 method [50], which is composed of two  
 179 modules: McClear v3 for clear-skies [51, 52] and McCloud for cloudy-skies [50]. The McClear  
 180 approach, version 3, used by CAMS radiation service, has been upgraded from McClear v2 and now  
 181 consist in a physical modelling using the radiative transfer model libRadtran [53]. As for the  
 182 MDSSFTD method, the McClear v3 now also relies on aerosols content and load, as well as gases  
 183 contents forecasted by ECMWF and distributed by CAMS. Compared to MDSSFTD method, McClear  
 184 v3 uses a monthly-climatology [54] of the MODIS surface albedos [55] and a similar approach than  
 185 MDSSFTD for the aggregation of the optical depths of each aerosol species to derive the properties  
 186 of the aerosol mixture [52]. The McCloud method estimates the cloud properties from MSG  
 187 measurements using a model adapted from APOLLO (AVHRR Processing scheme Over cLOUDs,  
 188 Land and Ocean, [56, 57].

189 For our validation analysis, we used the CAMS global and diffuse radiation data, at a temporal  
 190 resolution of 15-minutes. For sake of consistency with the evaluation against ground measurements,  
 191 the product was extracted for the whole validation period (February to October 2017) at the location  
 192 of the four BSRN stations already considered for the ground measurements analysis (Carpentras, De  
 193 Aar, Tamanrasset and Toravere).

#### 194 2.4. Metrics

195 The target accuracy metrics used are the Mean Bias Error (MBE) for low values of DSSF  
 196 (<200Wm<sup>-2</sup>) or of fd (<0.5). The target accuracy metrics used are the relative MBE (rMBE) for high  
 197 values of DSSF (>=200Wm<sup>-2</sup>) or of fd (>=0.5). MBE is computed as

$$198 MBE = \frac{1}{N} \times \sum_{i=1}^N (satelliteproduct_i - reference_i)$$

199 and the relative MBE, noted "rMBE" is a dimensionless metric, expressed in percent units, and  
 200 defined as:

$$201 rMBE = \frac{1}{N} \times \sum_{i=1}^N \frac{satelliteproduct_i - reference_i}{reference_i}$$

202 where N is the number of points and 'reference' corresponds to the ground measurements in our  
 203 study.

204 The choice of the metrics was made to ensure consistency with the two other existing LSA-SAF  
 205 products MDSSF and DIDSSF (LSA-201 and 203; see Section 0) for which the same evaluation strategy  
 206 was used. The ground measurements are separated into clear and cloudy samples based on the  
 207 information contained in the cloud mask. For example, if the SEVIRI pixel is defined as cloudy  
 208 (respectively clear) according to the information contained in the quality flag, the corresponding time  
 209 slot is then defined as cloudy (respectively clear) for the ground measurements. In the case of clear  
 210 sky retrievals, the clear sky pixel is excluded when the adjacent time slots (up to 1h, that is, 30 minutes  
 211 before and 30 minutes after) are defined as cloudy. This is deemed to suppress any residual cloud  
 212 contamination (or cloud shadow effects) in the clear sky retrievals. Same strategy is applied reversely  
 213 to identify cloudy-sky pixels with adjacent time slots which are clear-sky.

214 The aimed requirements are the target accuracies (values in bold Table 1). These metrics will be  
215 used in the following to evaluate the performances of the MDSSFTD product for clear-sky, cloudy-  
216 sky, and all-sky conditions. However, the user needs expressed to EUMETSAT is to have a MDSSFTD  
217 product which meets the target requirements for the all-sky conditions (without distinction according  
218 to cloudiness). The performances are evaluated based on the metrics that are obtained from all the  
219 available ground measurements (i.e., for all the stations and over the entire period of evaluation). The  
220 MDSSFTD product has the spatial resolution of the native SEVIRI grid (3km at the sub-satellite point  
221 over Africa and around 5km over Europe). [58] show that there is no major representativeness issue  
222 between the local ground-based solar radiation measurements and the satellite estimates (which have  
223 kilometer scales).

224 The evaluation is performed over a period of seven months: from February to October 2017.  
225 The stability of the metrics is also examined by splitting on a daily basis the metrics and analysing  
226 stability of the metrics from day to day.

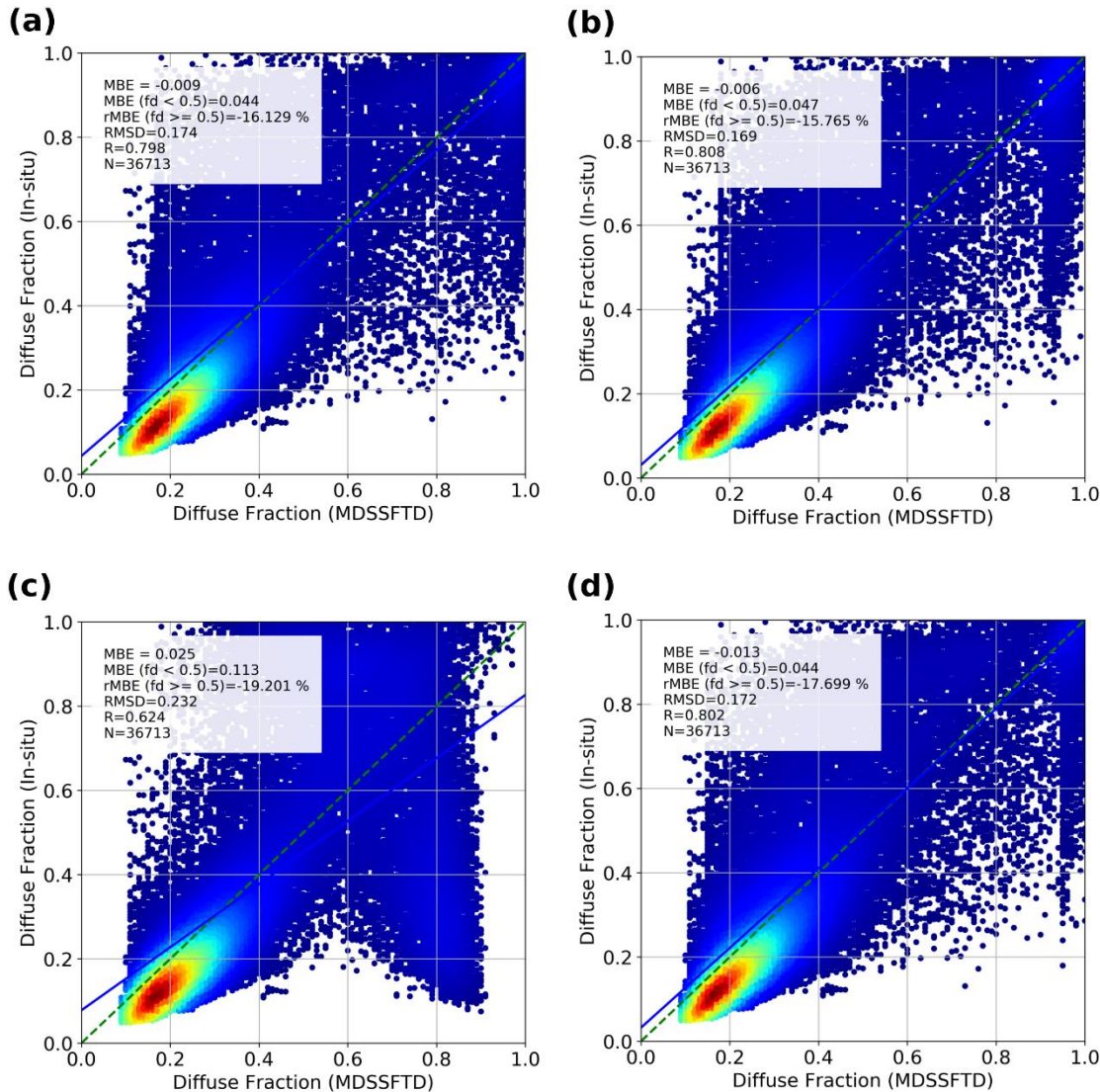
## 227 3. Results

### 228 3.1. *Sensitivity study: inter-comparison of models to estimate diffuse flux in cloudy-sky conditions*

229 A critical module in the method used for MDSSFTD is the choice of the empirical formulation  
230 used to estimate the diffuse fraction in the cloudy-sky case. In this context, a specific sensitivity study  
231 is first made to compare a set of existing solutions. One shall note that this sensitivity study only  
232 reflects the impact of the parametrisation choice on the diffuse fraction retrieval under cloudy  
233 conditions. Retrieval of the diffuse fraction under clear sky remains unchanged (see [40]).

234 We detail here this sensitivity study that compared several empirical formulations from the  
235 literature. The different formulations are based on [59-61]. All three methods estimate the diffuse part  
236 of the total solar irradiance from the clearness index (' $K_t$ '). This allows the calculation of the diffuse  
237 fraction by simply dividing the diffuse flux by the total counterpart. Another formulation based on  
238 [62] was also considered in this sensitivity study (Section 0). This fourth method, however, estimates  
239 the direct component of the solar irradiance based on ' $K_t$ ', which is used to infer the direct fraction  
240 of the solar irradiance to finally retrieve the diffuse fraction.

241 Figure 2 displays the density scatter plots for the diffuse fraction retrieved following each of the  
242 four formulations mentioned above, all compared to the *in-situ* diffuse fraction in all-sky conditions  
243 (clear and cloudy). The statistics shown in Figure 2 are obtained considering the four stations over  
244 the entire period of the study. As it can be seen, the statistics from the four formulations are highly  
245 similar, with slightly lower performances for the method from [62]. Because formulation based on  
246 [60] was validated against several stations over Europe and USA, we decided to use this formulation  
247 for our application. Indeed, the other models were derived from flux measurements over more  
248 limited areas, which make them less representative at the continental scale made possible by MSG.



249      **Figure 2** Diffuse fraction components retrieved following four empirical formulations, a) Erbs et al.,  
 250      b) Orgill and Hollands c) Louche et al., d) Reindl et al., and compared to the *in-situ* diffuse fraction  
 251      component. Blue color corresponds to low density of points and red color corresponds to high density  
 252      of points. Blue line represents the mean fit across the whole evaluation data.

253      *3.2. Diurnal comparisons for clear-sky and all-sky days*

254      The diurnal total and diffuse down-welling surface flux components from the MDSSFTD  
 255      product are compared against the same flux components derived from the ground BSRN  
 256      measurements. As already mentioned, the BSRN data (available at a high temporal frequency) are  
 257      averaged over 15 minutes and centred around the correct MSG acquisition time slot (see Section 0).

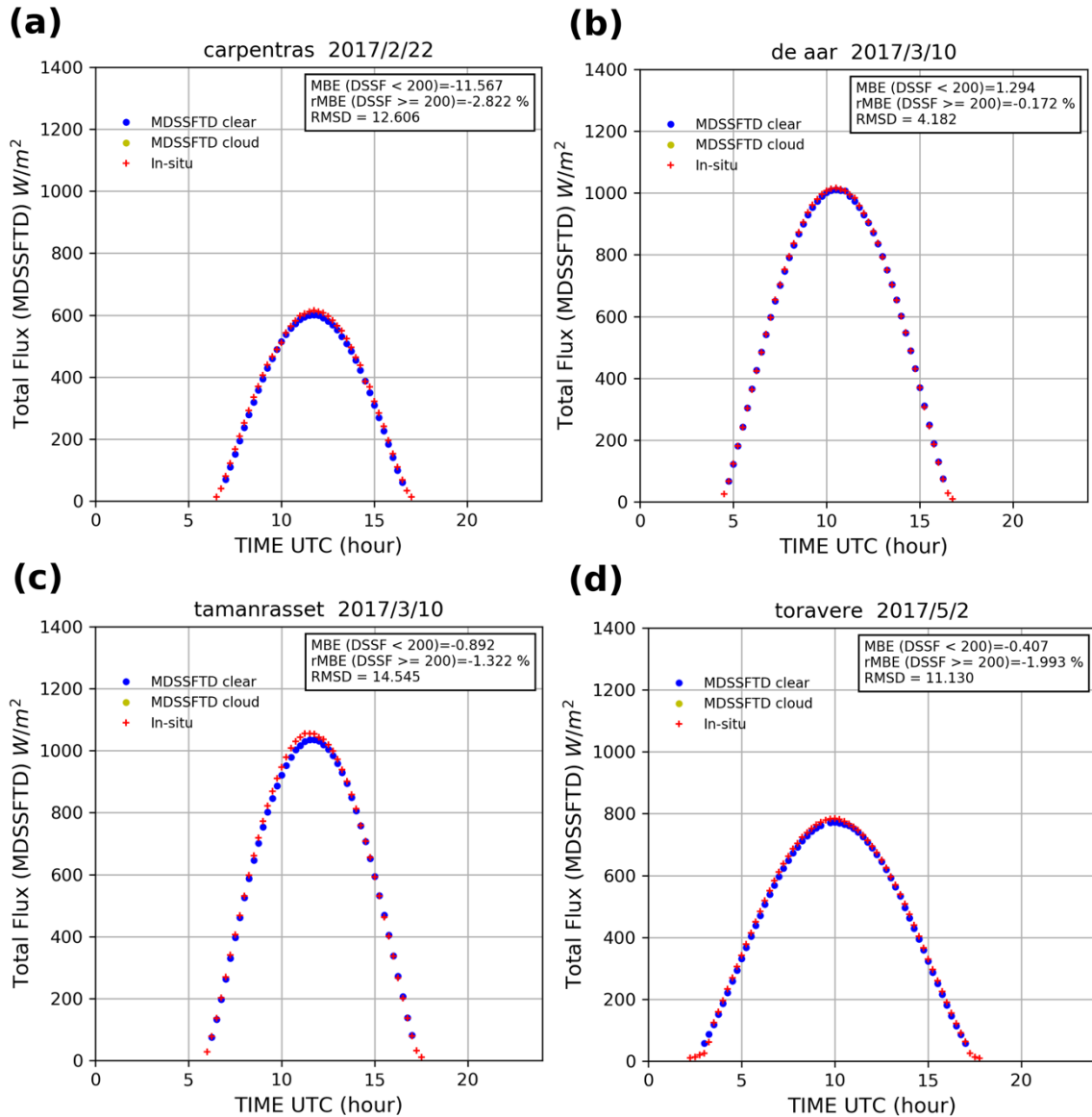
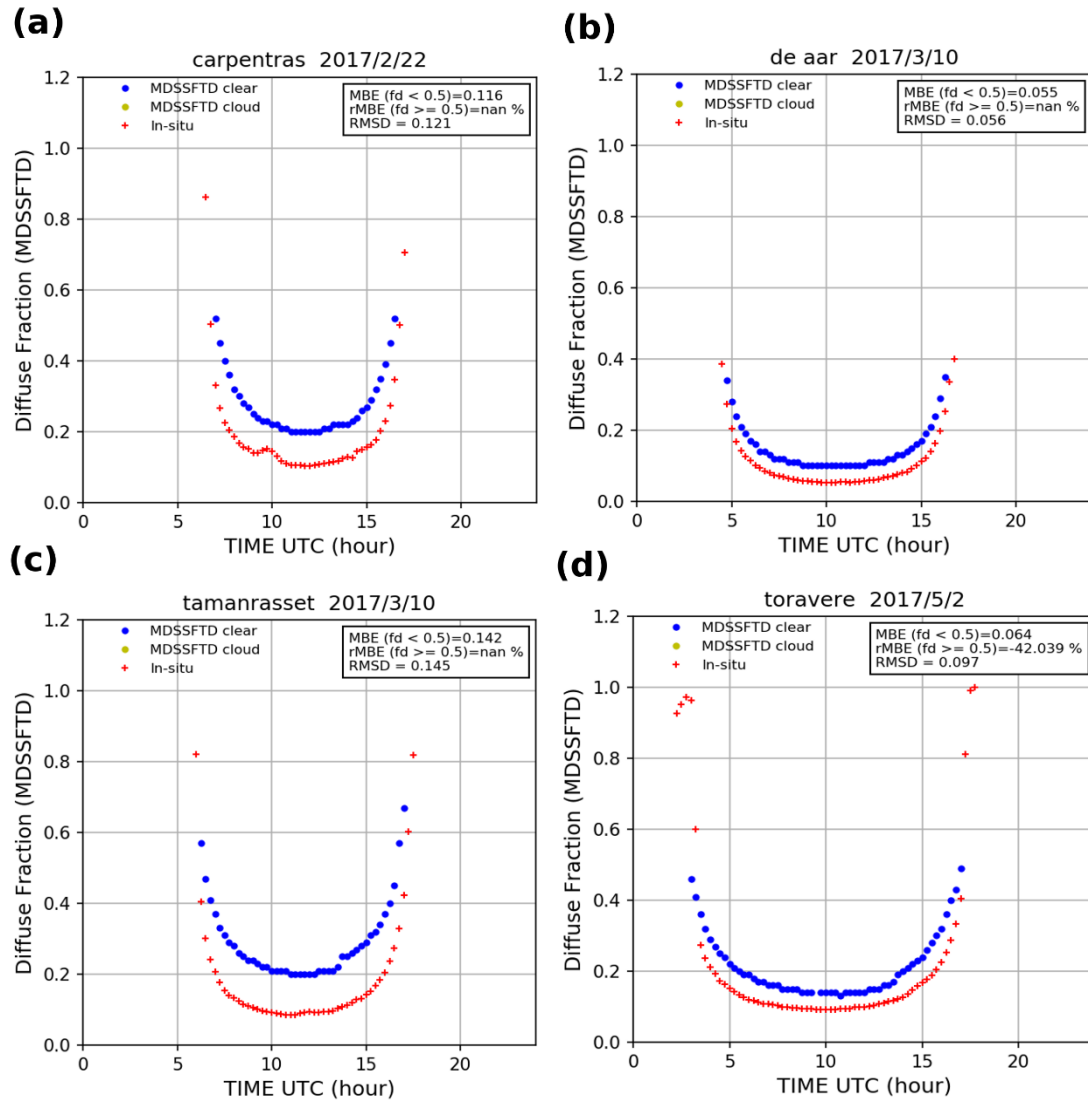


**Figure 3** Diurnal variation of the total MDSSFTD component in clear sky conditions compared against *in-situ* measurements for **a**) Carpentras, **b**) De Aar, **c**) Tamanrasset, and **d**) Toravere for a selected day. Yellow cloudy samples do not appear in this figure as the chosen dates were fully clear.



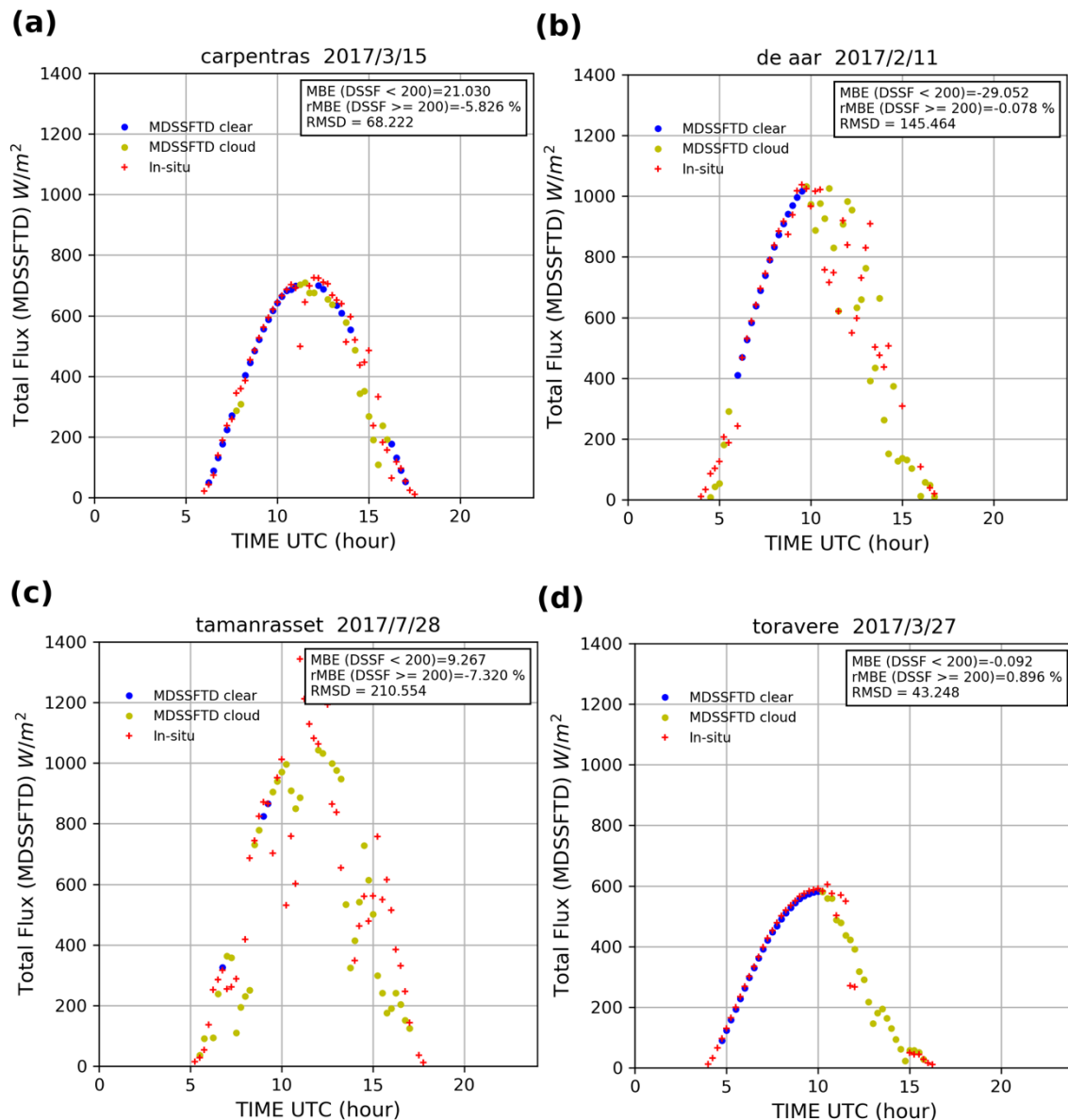
259      **Figure 4** Diurnal variation of the diffuse fraction MDSSFTD component in clear sky conditions  
 260      compared against *in-situ* measurements for **a)** Carpentras, **b)** De Aar, **c)** Tamanrasset, and **d)** Toravere  
 261      for a selected day. Yellow cloudy samples do not appear in this figure as the chosen dates were fully  
 262      clear.

263      Figure 3 shows a comparison between satellite-derived estimates and ground measurements of  
 264      the diurnal cycle of the total flux for clear sky conditions all along the day. It can be observed how  
 265      the satellite-derived estimates capture well the diurnal variations compared to ground measurements.

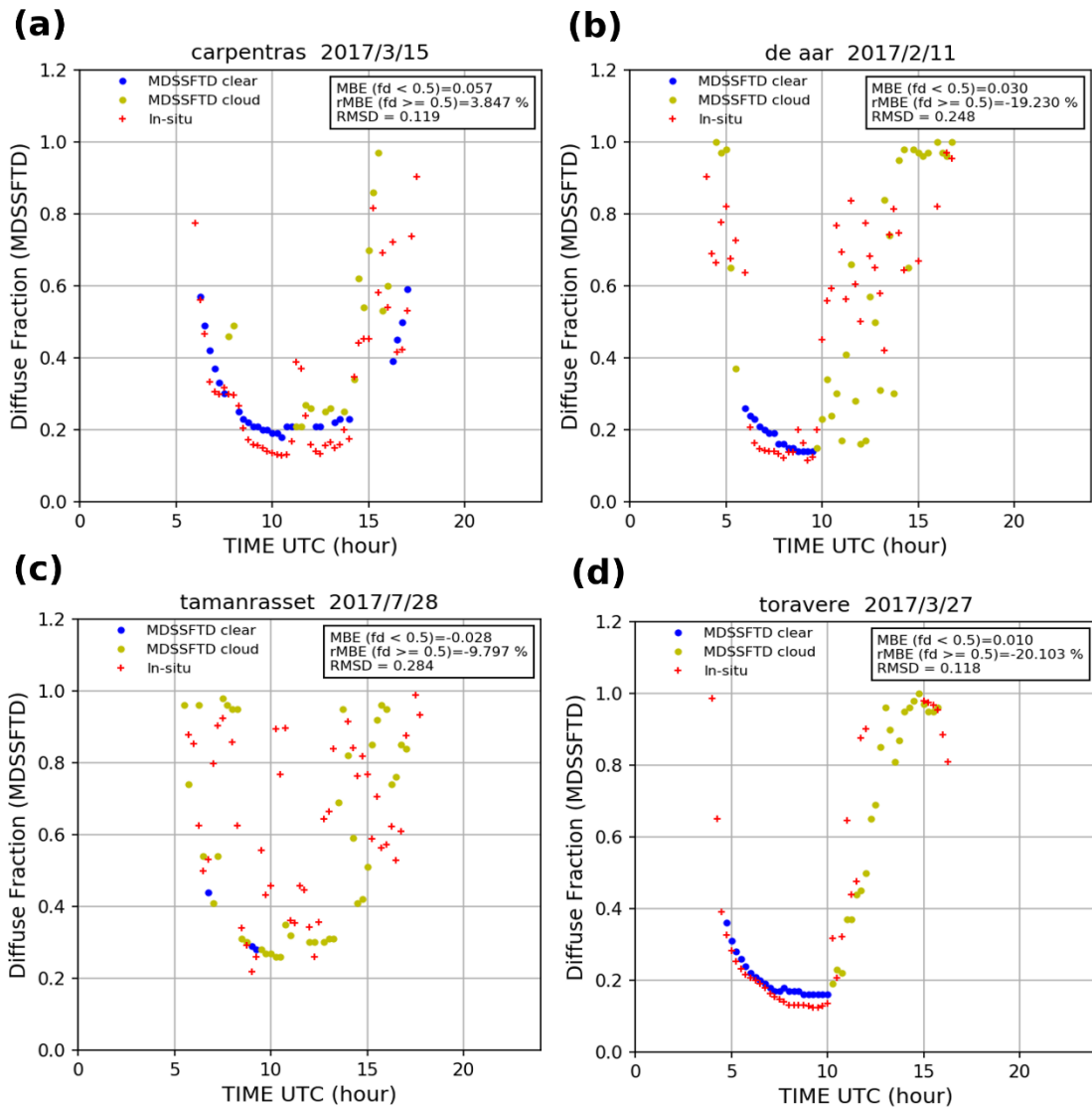
266      Figure 4 shows a comparison between satellite-derived estimates and ground measurements of  
 267      the diurnal cycle of the diffuse fraction for clear sky conditions. Again, the satellite-derived estimates  
 268      capture well the diurnal variations compared to ground measurements. In particular, the increase of  
 269      the diffuse fraction with extreme geometries is well reproduced. For these four days, a slight  
 270      overestimation between 0.055 and 0.142 is found for  $fd < 0.5$  in clear-sky conditions. This  
 271      overestimation comes from the slight overestimation of the diffuse DSSF by MDSSFTD, which was  
 272      also found for clear sky situations by [41] when using SIRAMix and the McClear method [51]. These  
 273      two methods used CAMS aerosol data and GADS aerosol properties, which may point to an  
 274      overestimation of the highly scattering aerosol components by CAMS or a limited transformation  
 275      from CAMS to GADS components.

276      Figures 5 and 6 show the results of similar comparisons that were conducted for dates showing  
 277      all sky conditions (partially clear and partially cloudy). The diurnal variations of the MDSSFTD

278 product, including the total DSSF and the diffuse fraction, are compared against ground  
 279 measurements for selected days in Figures 5 and 6, respectively. A rather satisfactory agreement  
 280 exists between the satellite derived estimates and the ground measurements. The increase of the  
 281 diffuse fraction with the cloudiness is generally well represented (e.g., see Figure 6 d).



282 **Figure 5** Diurnal variation of the total MDSSFTD component in all sky conditions compared against  
 283 *in-situ* measurements for **a**) Carpentras, **b**) De Aar, **c**) Tamanrasset, and **d**) Toravere for a selected day  
 284 (partially clear and cloudy). The yellow dots represent cloudy retrievals and the blue dots represent  
 285 clear sky retrievals.



286      **Figure 6** Diurnal variation of the diffuse fraction of MDSSFTD in all sky conditions compared  
 287      against *in-situ* measurements for **a**) Carpentras, **b**) De Aar, **c**) Tamanrasset, and **d**) Toravere for a  
 288      selected days (partially clear and cloudy). The yellow dots represent cloudy retrievals and the blue  
 289      dots represent clear sky retrievals.

290      **3.3. Global performances**

291      This section details the overall statistics of the MDSSFTD product that are obtained by  
 292      considering the evaluation over the four ground stations for the entire period of interest, with  
 293      temporal frequency of every 15min. Statistics are hence discussed successively for clear-sky, cloudy-  
 294      sky, and all-sky conditions.

295      **3.3.1. Clear-sky conditions**

296      Figure 7 displays the density scatter plot between instantaneous measurements of MSG-derived  
 297      surface down-welling solar flux measurements for total and diffuse fraction components with their  
 298      *in-situ* counterparts. Only clear sky retrievals are considered here thanks to the use of the cloud mask  
 299      used as input in the MDSSFTD algorithm. Figure 7 shows that the satellite estimates of DSSF and fd  
 300      meet the requirements for total DSSF, which are  $20\text{Wm}^{-2}$  for  $\text{DSSF} < 200\text{Wm}^{-2}$  and 10% for  
 301       $\text{DSSF} \geq 200\text{Wm}^{-2}$  (as described in Table 1). The MBE and rMBE compared to the ground  
 302      measurements are  $8.637\text{Wm}^{-2}$  and 0.776%, respectively. On the other hand, the requirements for fd  
 303      measurements are  $8.637\text{Wm}^{-2}$  and 0.776%, respectively. On the other hand, the requirements for fd

304 are 0.1 for  $fd < 0.5$  and 20% for  $fd \geq 0.5$ . The MBE and rMBE compared to the ground measurements in  
 305 this case are 0.062 and -22.197%, respectively. The statistical scores in terms of MBE and RMSD (root  
 306 mean square deviation) for the comparison between MDSSFTD total and diffuse fraction components  
 307 with their *in-situ* counterparts for all four stations are given in Tables 2 and 3. The scores for all  
 308 stations are in agreement with the DSSF product requirements. The diffuse fraction compares well  
 309 for all stations except for high values of diffuse fraction ( $fd \geq 0.5$ ). However, only 12 days over the 7-  
 310 month period of the study have  $fd \geq 0.5$  in clear-sky conditions (see Figure 13). Indeed, these values  
 311 of diffuse fraction correspond to intense aerosol loading, which is relatively infrequent. Therefore,  
 312 statistics in that case ( $fd \geq 0.5$  and clear-sky conditions) cannot be considered as significant from a  
 313 statistical point of view.

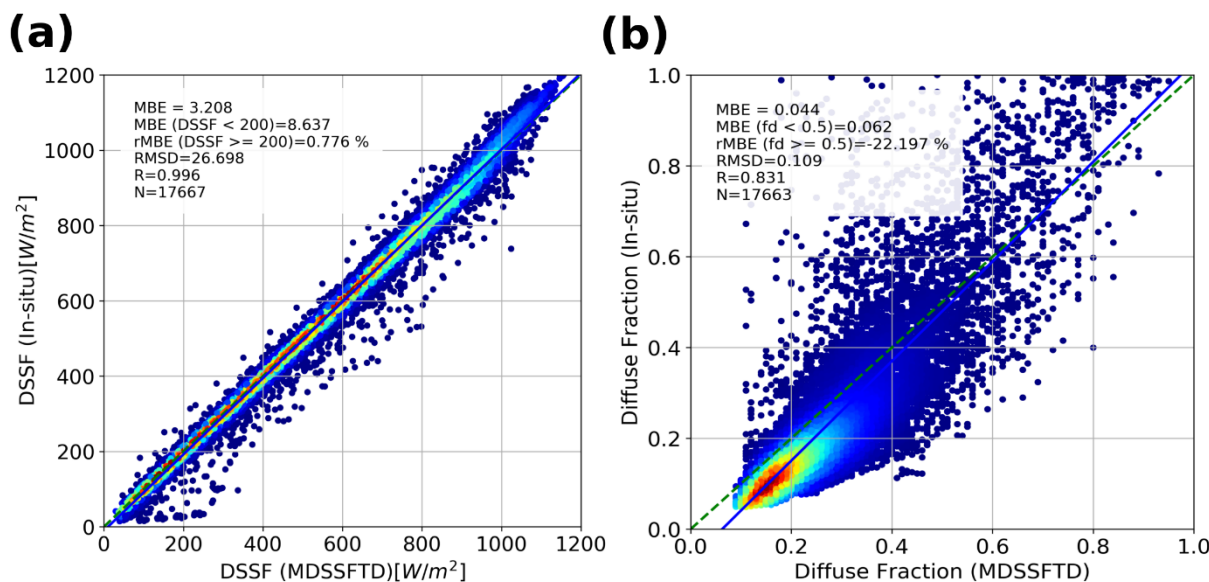


**Figure 7** Comparison of instantaneous MSG-derived MDSSFTD measurements for (a) total DSSF, (b) diffuse fraction components with their *in-situ* counterparts for clear-sky retrievals. The retrievals are collected every 15 min. Blue line represents the mean fit across the whole evaluation data. Blue circles corresponds to low density of points and red circles corresponds to high density of points.

314 **Table 2** Statistical scores obtained from the comparison between MDSSFTD derived total flux  
 315 estimates and ground *in-situ* measurements over the selected BSRN sites for clear sky retrievals. If the  
 316 value is in bold, the metric does not meet the “target” requirements. If no value appears in bold, all  
 317 the metrics meet the requirements. R\_VAL correspond to the Pearson correlation coefficient. RMSD  
 318 is the root mean square deviation.

|             | Lat °N | Lon °E | R_VAL [-] | RMSD [Wm <sup>-2</sup> ] | MBE [Wm <sup>-2</sup> ] | MBE (DSSF<200) [Wm <sup>-2</sup> ] | rMBE (DSSF>=200) [%] |
|-------------|--------|--------|-----------|--------------------------|-------------------------|------------------------------------|----------------------|
| Carpentras  | 44.08  | 5.06   | 0.998     | 22.809                   | 14.552                  | 6.759                              | 2.623                |
| De Aar      | -30.67 | 23.99  | 0.996     | 23.042                   | -2.946                  | 8.927                              | -0.797               |
| Tamanrasset | 22.79  | 5.53   | 0.995     | 34.096                   | -0.441                  | 12.336                             | 0.798                |
| Toravere    | 58.25  | 26.46  | 0.996     | 19.277                   | 1.488                   | 4.297                              | 0.320                |

319 **Table 3** Statistical scores obtained from the comparison between MDSSFTD diffuse fraction estimates  
 320 and ground measurements over the selected BSRN sites for clear sky retrievals. If the value is in bold,  
 321 the metric does not meet the “target” requirements. If no value appears in bold, all the metrics meet

322  
323

the requirements.  $R_{VAL}$  correspond to the Pearson correlation coefficient. RMSD is the root mean square deviation.

|             | Lat °N | Lon °E | $R_{VAL}$<br>[-] | RMSD<br>[-] | MBE<br>[-] | MBE (fd<0.5)<br>[-] | rMBE (fd>=0.5)<br>[%] |
|-------------|--------|--------|------------------|-------------|------------|---------------------|-----------------------|
| Carpentras  | 44.08  | 5.06   | 0.890            | 0.069       | 0.042      | 0.045               | -10.173               |
| De Aar      | -30.67 | 23.99  | 0.624            | 0.115       | 0.065      | 0.073               | <b>-47.698</b>        |
| Tamanrasset | 22.79  | 5.53   | 0.831            | 0.134       | 0.028      | 0.072               | <b>-21.216</b>        |
| Toravere    | 58.25  | 26.46  | 0.768            | 0.091       | 0.027      | 0.039               | <b>-31.354</b>        |

324 3.3.2. Cloudy-sky conditions

325 Figure 8 displays the density scatter plot between instantaneous measurements of MSG-derived  
326 surface down-welling solar flux measurements for total and diffuse fraction components with their  
327 *in-situ* counterparts. Only cloudy sky retrievals are considered for this experiment. Figure 8 shows  
328 that the satellite estimates of DSSF and fd meet the target requirements. For DSSF, the requirements  
329 are  $20\text{Wm}^{-2}$  for  $\text{DSSF} < 200\text{Wm}^{-2}$  and 10% for  $\text{DSSF} \geq 200\text{Wm}^{-2}$ . The MBE and rMBE compared to the  
330 ground measurements are  $-6.618\text{Wm}^{-2}$  and  $-2.782\%$ , respectively. For fd, the requirements are 0.1 for  
331  $\text{fd} < 0.5$  and 20% for  $\text{fd} \geq 0.5$ . The MBE and rMBE compared to the ground measurements are 0.027 and  
332  $-15.796\%$ , respectively. Tables 4 and 5 give the statistical scores in terms of MBE and RMSD for the  
333 comparison between MDSSFTD total and diffuse fraction components with their *in-situ* counterparts  
334 for all four stations. The vertical patterns that are observed in Figure 8(b) comes from the method that  
335 is used for cloudy skies. Indeed, the estimation of the diffuse fraction is estimated using three  
336 equations that are selected according to the value of clearness index. More details are given in the  
337 companion paper [40].

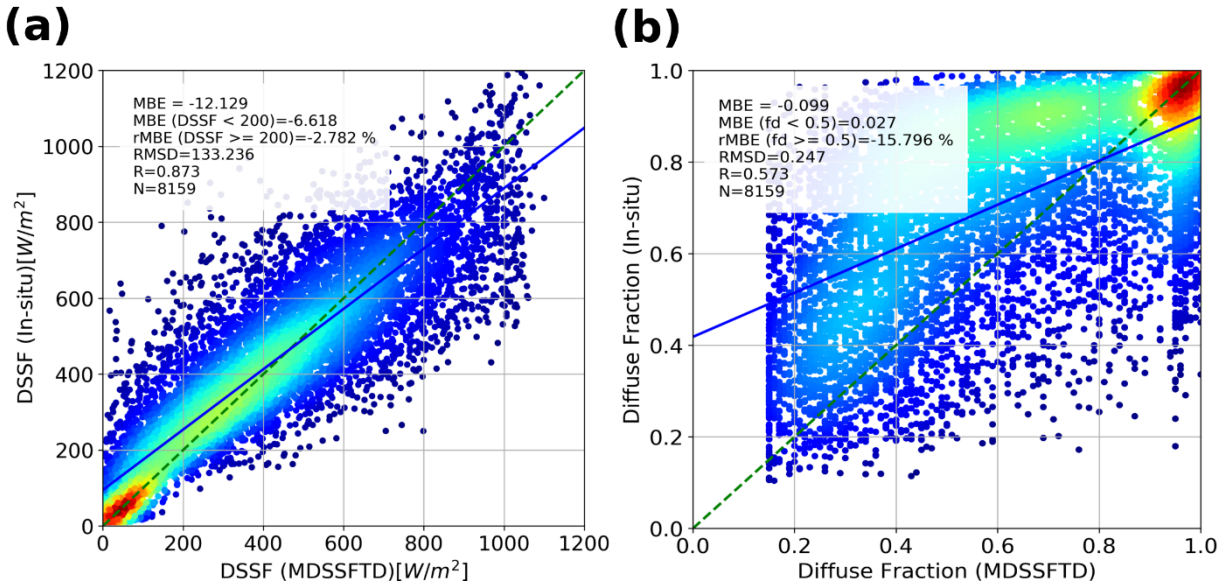


**Figure 8** Comparison of instantaneous MSG-derived MDSSFTD measurements for (a) total, (b) diffuse fraction components with their *in-situ* counterparts for cloudy-sky retrievals. The retrievals are collected every 15 min. Blue line represents the mean fit across the whole evaluation data. Blue circles corresponds to low density of points and red circles corresponds to high density of points.

338  
339

**Table 4** Statistical scores obtained from the comparison between MDSSFTD total flux estimates and ground measurements over the selected BSRN sites for cloudy sky retrievals. If the value is in bold,

340  
341

the metric does not meet the “target” requirements. If no value appears in bold, all the metrics meet the requirements.

|             | Lat °N | Lon °E | R_VAL<br>[-] | RMSD<br>[Wm <sup>-2</sup> ] | MBE<br>[Wm <sup>-2</sup> ] | MBE (DSSF<200)<br>[Wm <sup>-2</sup> ] | rMBE (DSSF>=200)<br>[%] |
|-------------|--------|--------|--------------|-----------------------------|----------------------------|---------------------------------------|-------------------------|
| Carpentras  | 44.08  | 5.06   | 0.886        | 124.089                     | -5.226                     | -20.663                               | -1.463                  |
| De Aar      | -30.67 | 23.99  | 0.860        | 144.928                     | -22.573                    | -16.236                               | -5.585                  |
| Tamanrasset | 22.79  | 5.53   | 0.861        | 174.924                     | 54.220                     | <b>-21.255</b>                        | 10.806                  |
| Toravere    | 58.25  | 26.46  | 0.880        | 117.562                     | -34.572                    | 0.800                                 | -8.025                  |

342  
343  
344  
345

**Table 5** Statistical scores obtained from the comparison between MDSSFTD diffuse fraction estimates and ground measurements over the selected BSRN sites for cloudy sky retrievals. If the value is in bold, the metric does not meet the “target” requirements. If no value appears in bold, all the metrics meet the requirements.

|             | Lat °N | Lon °E | R_VAL<br>[-] | RMSD<br>[-] | MBE<br>[-] | MBE (fd<0.5)<br>[-] | rMBE (fd>=0.5)<br>[%] |
|-------------|--------|--------|--------------|-------------|------------|---------------------|-----------------------|
| Carpentras  | 44.08  | 5.06   | 0.620        | 0.246       | -0.108     | -0.047              | -15.082               |
| De Aar      | -30.67 | 23.99  | 0.489        | 0.287       | -0.109     | -0.007              | -17.631               |
| Tamanrasset | 22.79  | 5.53   | 0.418        | 0.306       | -0.198     | -0.079              | <b>-25.767</b>        |
| Toravere    | 58.25  | 26.46  | 0.647        | 0.215       | -0,060     | 0.064               | -11.693               |

## 346 3.3.3. All-sky (clear and cloudy) conditions

347 In a similar way, the total DSSF and diffuse fraction from the MDSSFTD product for all sky  
348 retrievals are compared against their *in-situ* counterparts in Figure 9. We remind that the metrics  
349 obtained for all-sky conditions are those that are used to evaluate the performances of the product in  
350 the framework of the LSA SAF program (see Section 0).

351 Figure 9 displays the density scatter plot between instantaneous measurements of MSG-derived  
352 surface downwelling solar flux measurements for total and diffuse fraction components with their  
353 *in-situ* counterparts for the all-sky retrievals. Figure 9 shows that the satellite estimates of DSSF and  
354 fd meet the requirements. For DSSF, the requirements are 20Wm<sup>-2</sup> for DSSF<200Wm<sup>-2</sup> and 10% for  
355 DSSF>=200Wm<sup>-2</sup>. The MBE and rMBE compared to the ground measurements are 3.618Wm<sup>-2</sup> and  
356 0.252%, respectively. For fd, the requirements are 0.1 for fd<0.5 and 20% for fd>=0.5Wm<sup>-2</sup>. The MBE  
357 and rMBE compared to the ground measurements are 0.044 and -17.699%, respectively. The statistical  
358 scores in terms of MBE and RMSD for the comparison between MDSSFTD total and diffuse fraction  
359 components with their *in-situ* counterparts for all four stations are given in Tables 6 and 7. The scores  
360 for all stations are in agreement with the MDSSFTD product requirements. The diffuse fraction  
361 compares well for most stations except in De Aar and Tamanrasset if a 20% threshold is considered  
362 for fd>0.5.

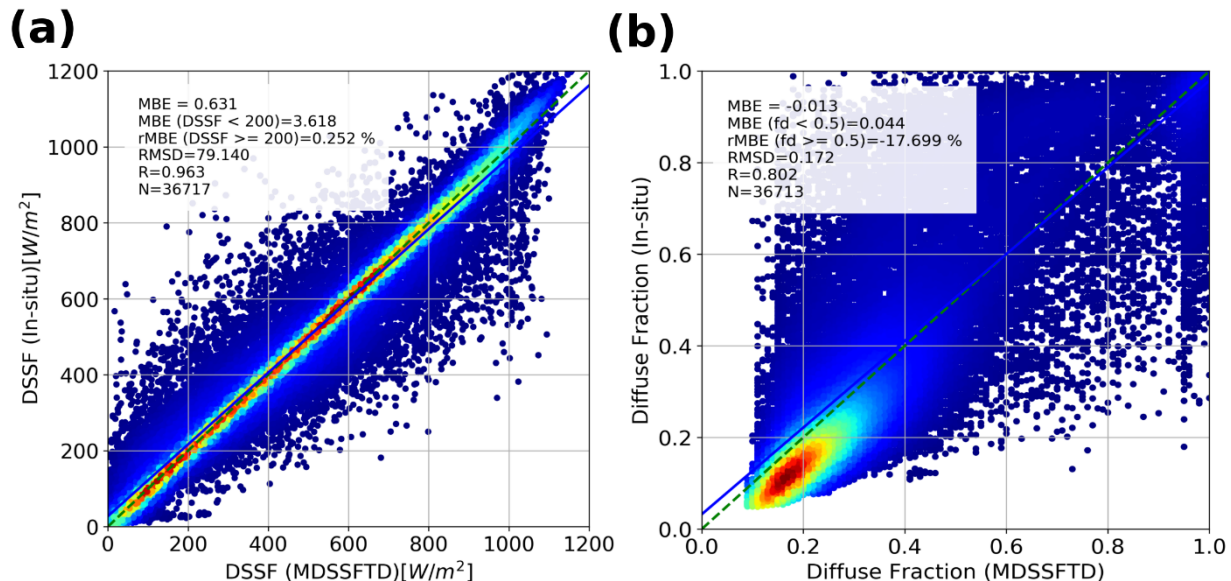


**Figure 9** Comparison of instantaneous MSG-derived MDSSFTD measurements for (a) total, (b) diffuse fraction components with their *in-situ* counterparts for all sky (clear and cloudy) retrievals. The retrievals are collected every 15 min. Blue line represents the mean fit across the whole evaluation data. Blue circles corresponds to low density of points and red circles corresponds to high density of points.

363  
364  
365  
366

**Table 6** Statistical scores obtained from the comparison between MDSSFTD total flux estimates and ground measurements over the selected BSRN sites for all (clear and cloudy) sky retrievals. If the value is in bold, the metric does not meet the “target” requirements. If no value appears in bold, all the metrics meet the requirements.

|             | Lat    | Lon   | R_VAL | RMSD                | MBE                 | MBE (DSSF<200)      | rMBE (DSSF>=200) |
|-------------|--------|-------|-------|---------------------|---------------------|---------------------|------------------|
|             |        |       | [-]   | [Wm <sup>-2</sup> ] | [Wm <sup>-2</sup> ] | [Wm <sup>-2</sup> ] | [%]              |
| Carpentras  | 44.08  | 5.06  | 0.969 | 69.584              | 10.790              | 0.728               | 2.037            |
| De Aar      | -30.67 | 23.99 | 0.969 | 64.833              | -4.015              | 5.891               | -0.993           |
| Tamanrasset | 22.79  | 5.53  | 0.965 | 86.075              | 10.722              | 5.034               | 2.939            |
| Toravere    | 58.25  | 26.46 | 0.917 | 94.607              | -18.026             | 3.604               | -4.125           |

367  
368  
369  
370

**Table 7** Statistical scores obtained from the comparison between MDSSFTD diffuse fraction estimates and ground measurements over the selected BSRN sites for all (clear and cloudy) sky retrievals. If the value is in bold, the metric does not meet the “target” requirements. If no value appears in bold, all the metrics meet the requirements.

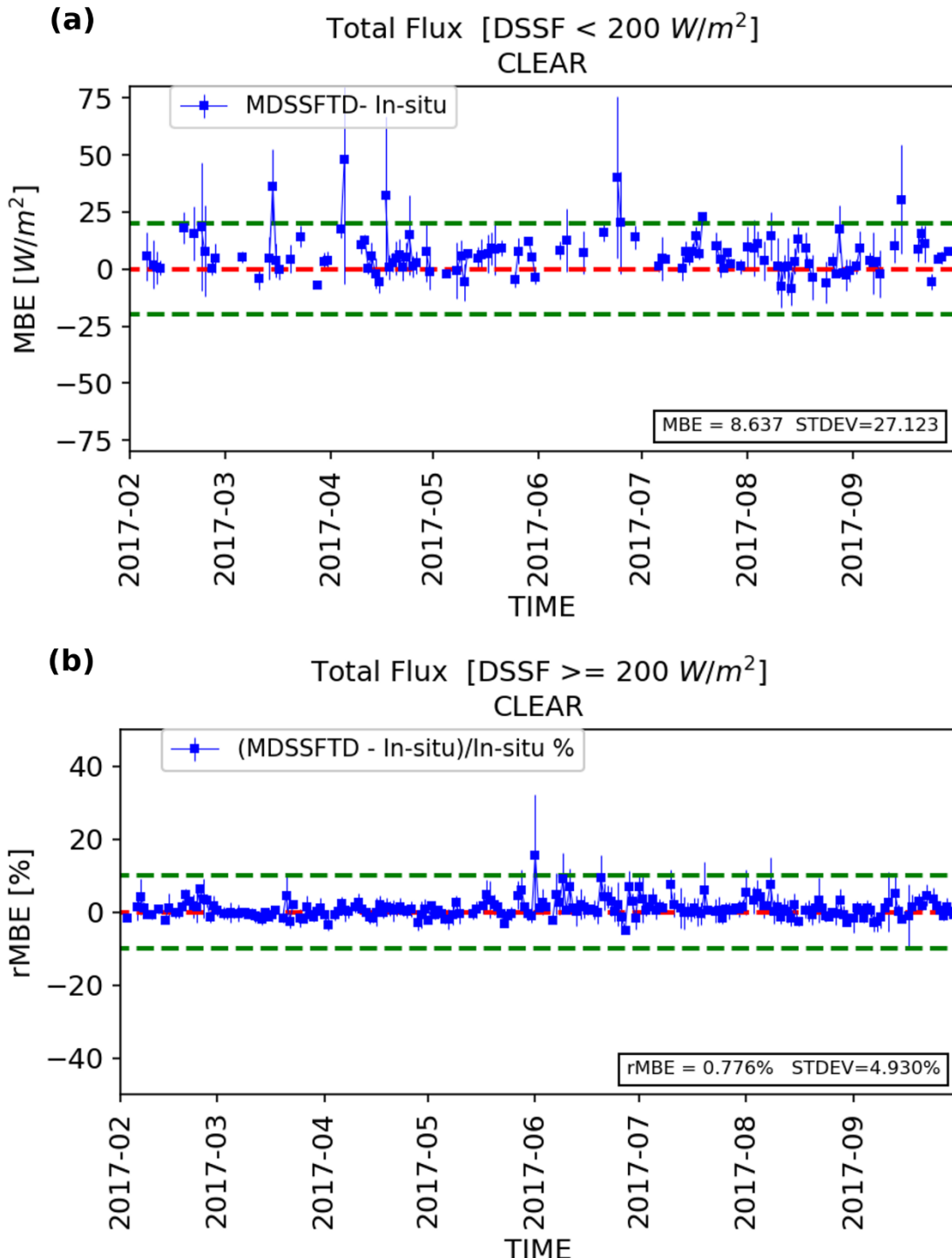
|             | Lat    | Lon   | R_VAL | RMSD  | MBE    | MBE (fd<0.5) | rMBE (fd>=0.5) |
|-------------|--------|-------|-------|-------|--------|--------------|----------------|
|             |        |       | [-]   | [-]   | [-]    | [-]          | [-]            |
| Carpentras  | 44.08  | 5.06  | 0.818 | 0.151 | -0.006 | 0.029        | -14.753        |
| De Aar      | -30.67 | 23.99 | 0.734 | 0.161 | 0.022  | 0.054        | <b>-21.809</b> |
| Tamanrasset | 22.79  | 5.53  | 0.755 | 0.184 | -0.034 | 0.057        | <b>-22.949</b> |
| Toravere    | 58.25  | 26.46 | 0.786 | 0.191 | -0.035 | 0.038        | -13.361        |

371

### 3.4. Stability of the metrics

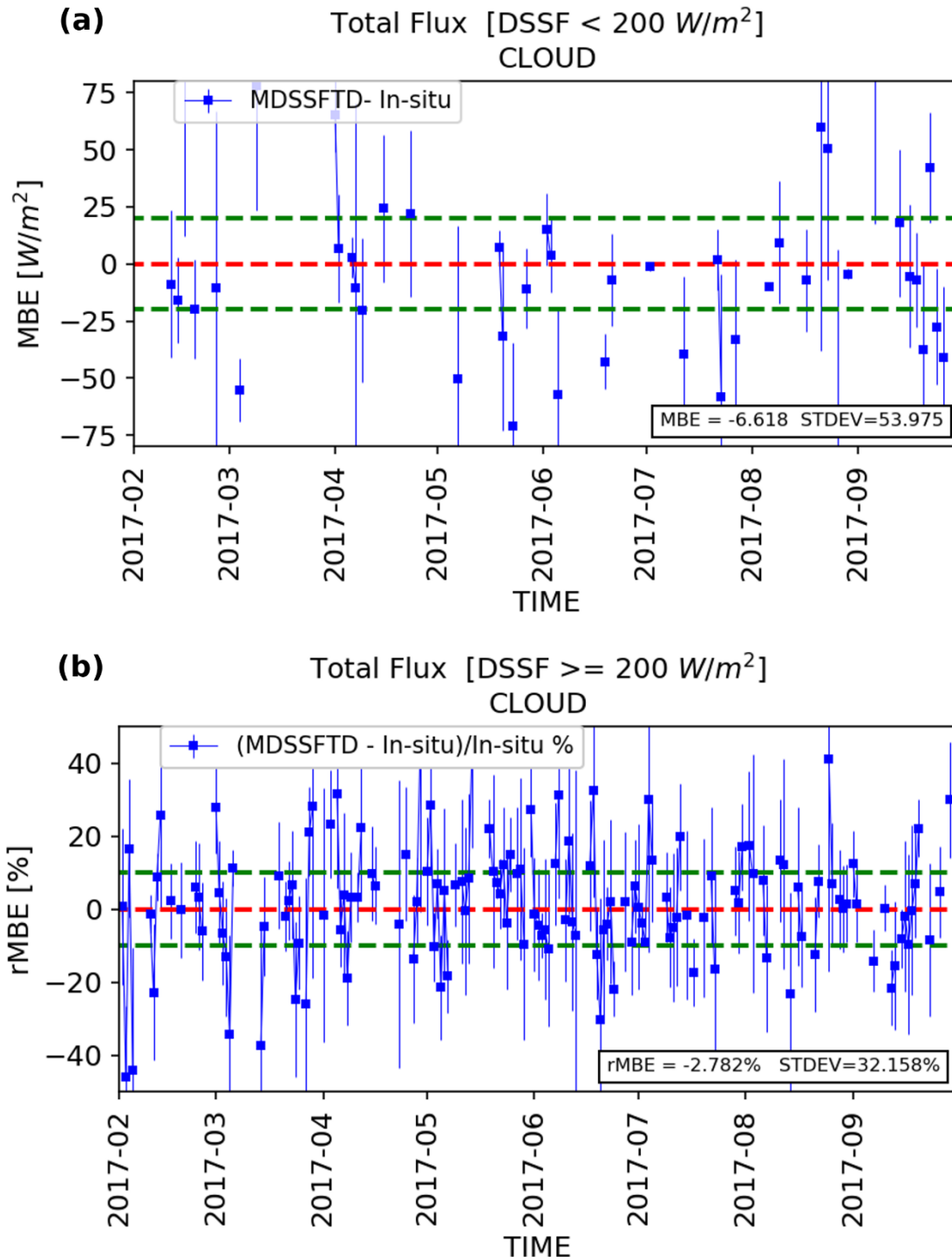
372 Here, we present the time series of the mean statistics averaged over all stations for the  
373 MDSSFTD total flux products (DSSF and fd). The goal is to study the temporal evolution of  
374 performances with time. The 15-min statistics between the 15-min satellite derived products and the  
375 15-min resampled ground measurements are averaged on a daily basis. Standard deviation of the 15-  
376 min statistics are also calculated on a daily basis and reported in the following plots. The statistics  
377 are calculated for both DSSF regimes and both outputs: for total flux, DSSF less than 200 Wm<sup>-2</sup> and  
378 greater than 200 Wm<sup>-2</sup>; and for the diffuse fraction, fd lower than 0.5 and greater than 0.5.

379 First, Figures 10 and 13 show the time series of the metrics for clear-sky conditions. Second,  
380 Figures 11 and 14 show the time series of the metrics for cloudy-sky conditions. Finally, Figures 12  
381 and 15 show the time series of the metrics for all-sky (clear and cloudy) conditions. All figures show  
382 the daily averages along with the standard deviation, which is related to the variation of values  
383 among the different stations. First, it is important to highlight that all these conditions do not have  
384 the same level of representativeness due to the varying number of samples in the different cases. The  
385 only case that frequently shows values going beyond the requirement limits (i.e. the horizontal green  
386 lines) is the cloudy-sky case for high values of fd (fd>=0.5; see Figure 14). In all the other conditions,  
387 and especially for all-sky (clear and cloudy) conditions, the average statistics obtained from the  
388 product outputs meet the target requirement along the entire period of the analysis.



389  
390  
391  
392  
393  
394

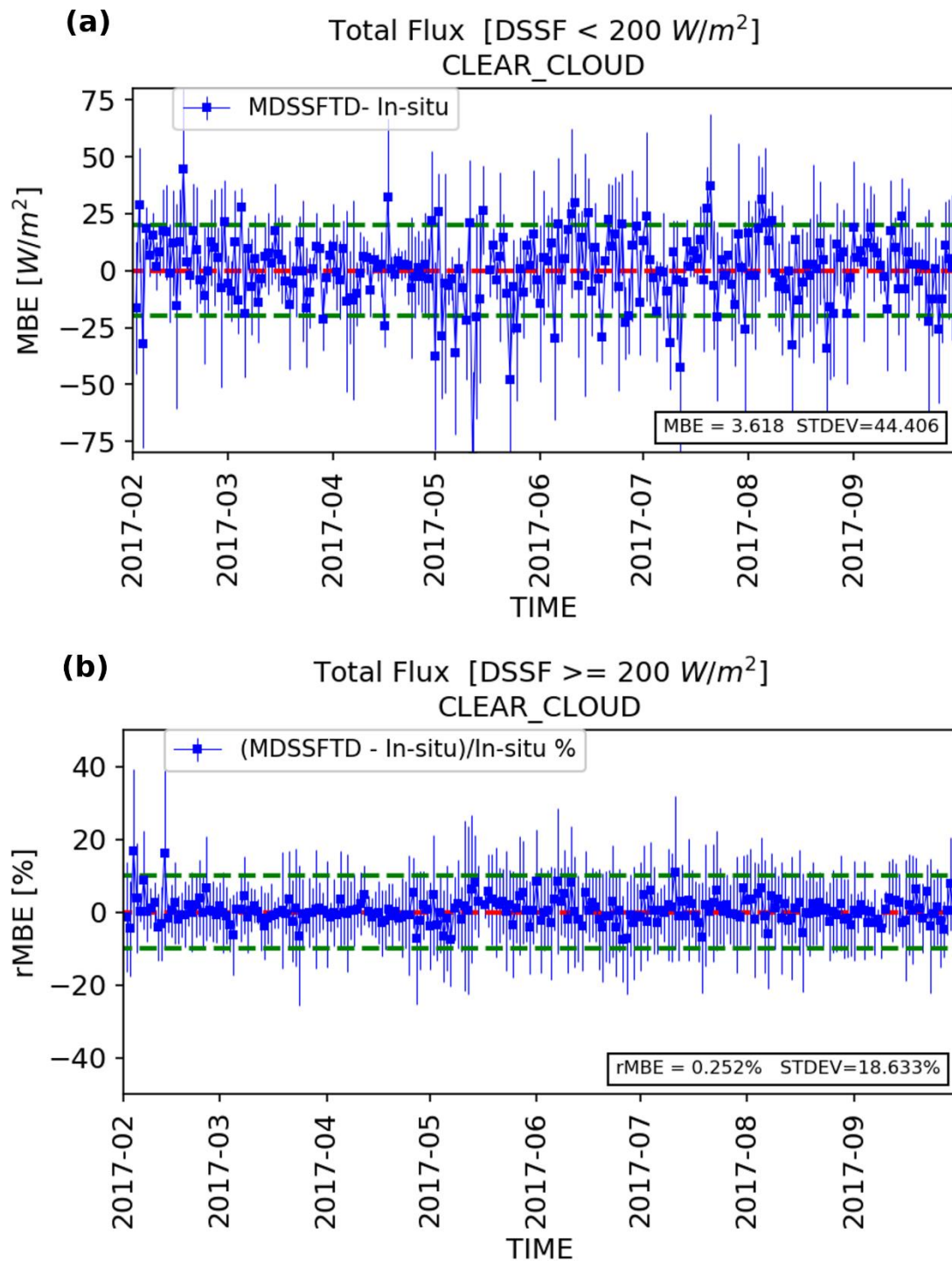
Figure 10 Time series of statistics of difference averaged on a daily basis between 15 min in-situ measurements and 15 min MDSSFTD total flux (blue dots). The daily standard deviation of the absolute and relative statistics are indicated with vertical blue lines. The data points are filtered to keep those a) total flux values less than 200 Wm<sup>-2</sup> (absolute statistics) and b) total flux values greater than 200 Wm<sup>-2</sup> (relative statistics). The comparison is made only for the clear-sky conditions. The green dotted horizontal lines characterize the “target” accuracy requirements.



395

**Figure 11** Same than Figure 10 for cloudy-sky conditions.

396



397

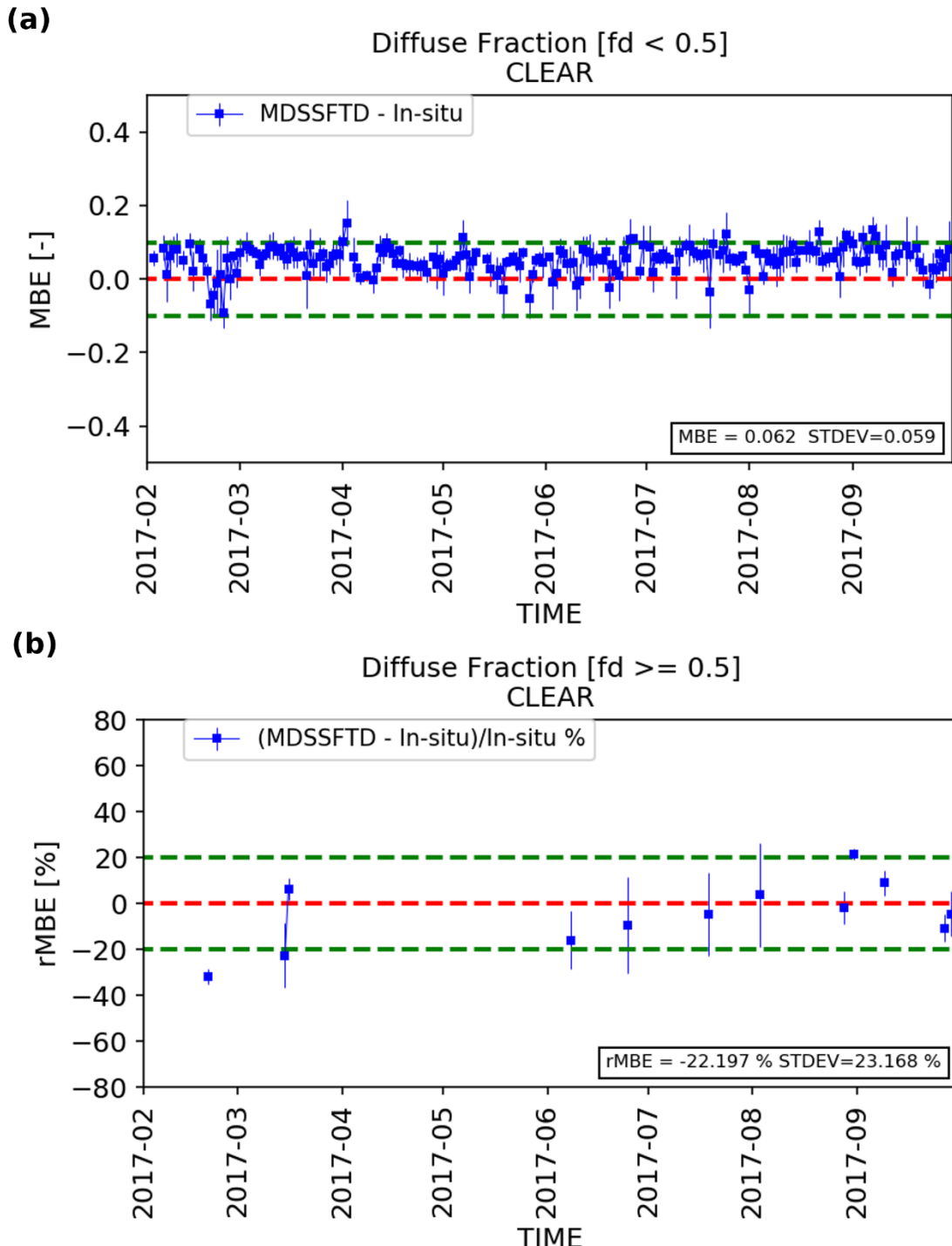
Figure 12 Same than Figure 10 for all-sky (clear and cloudy) conditions.

398

399

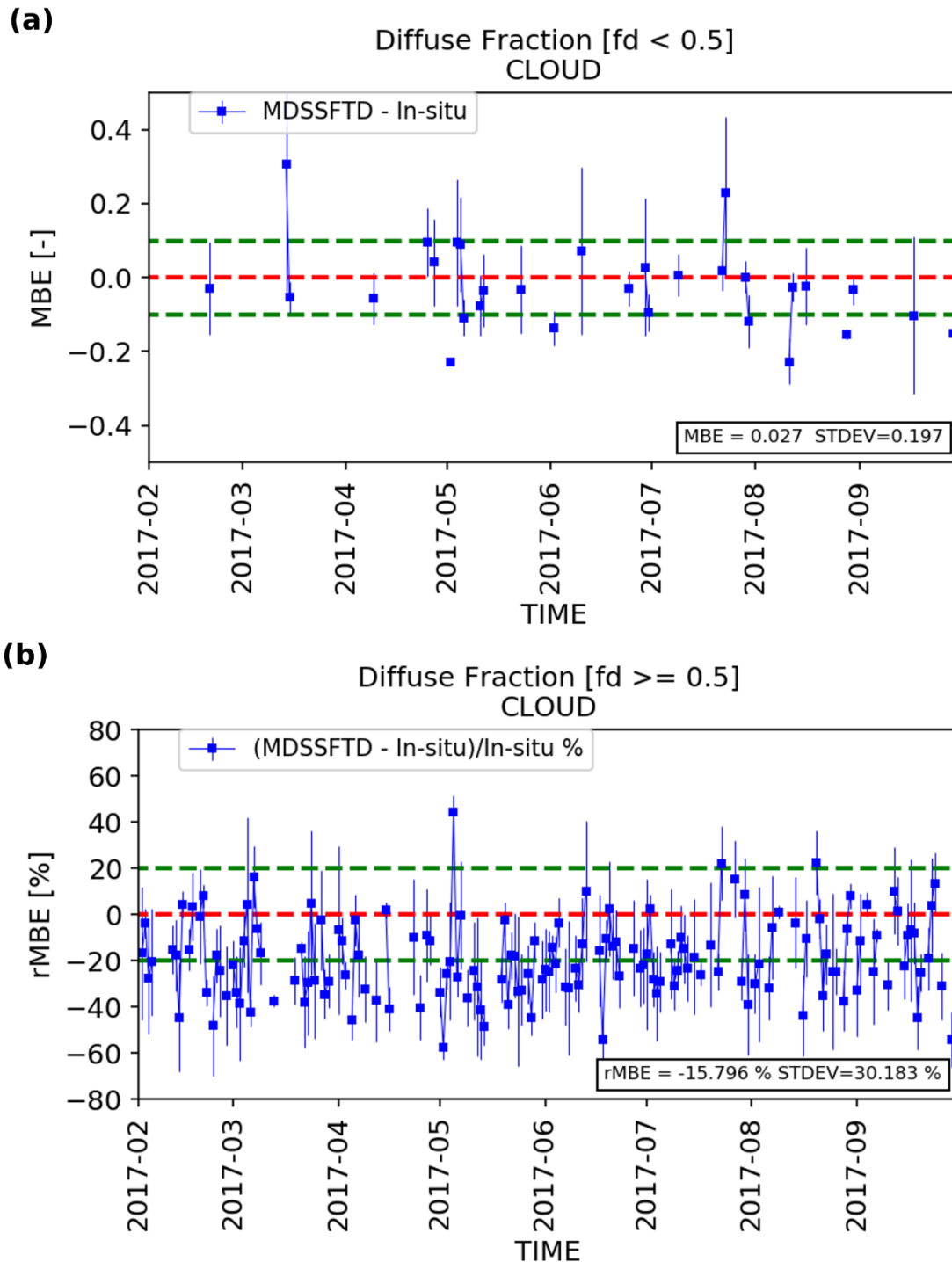
400

401



402  
403  
404  
405  
Figure 13 Time series of the relative mean bias for the comparison of the diffuse fraction on the 15  
minutes time step basis. Statistics of difference are averaged on a daily basis. The standard deviation  
of the relative statistics are indicated with vertical blue lines. The comparison is made only for clear-  
sky conditions. The green dotted horizontal lines characterize the “target” requirements.

406  
407



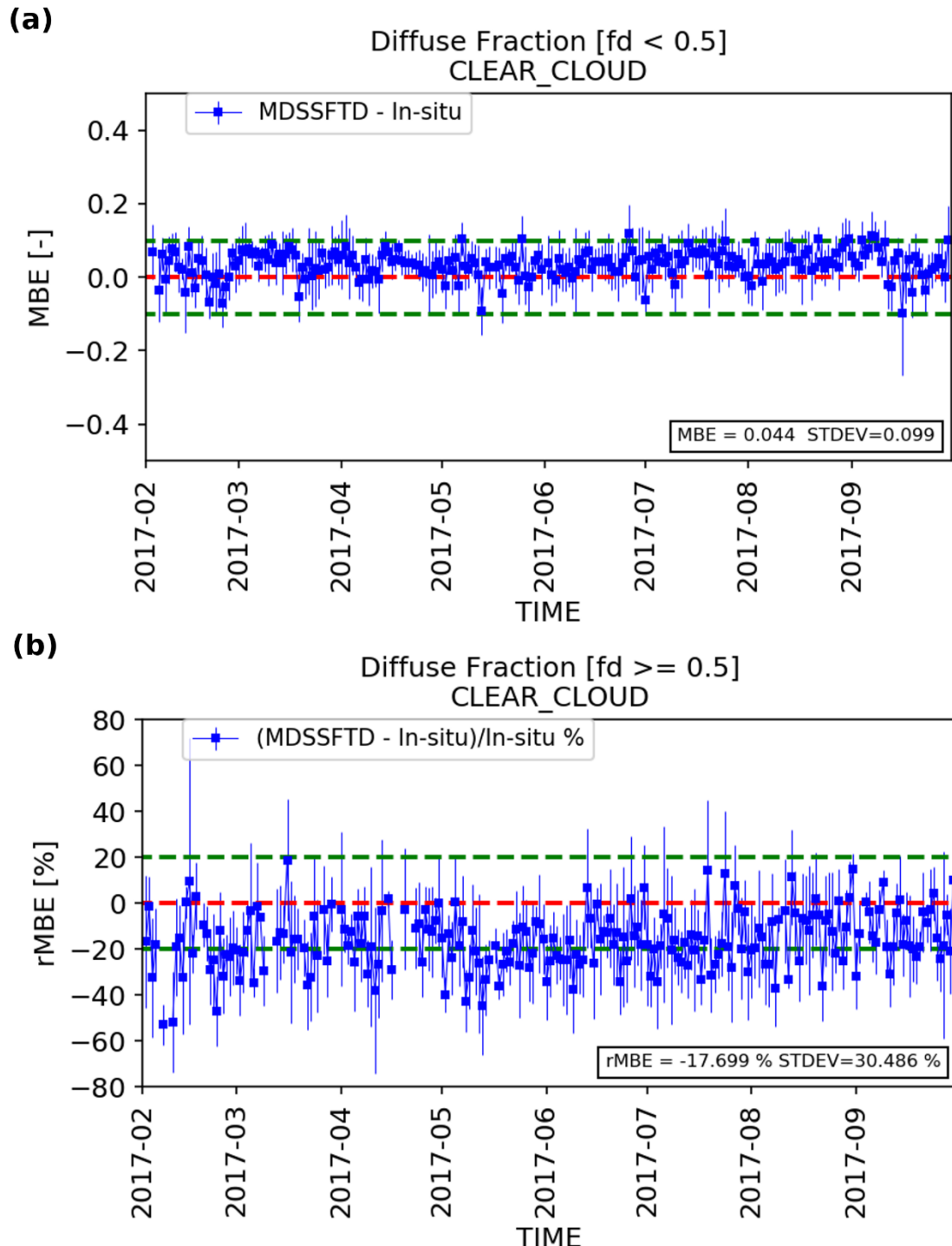
408

Figure 14 Same than Figure 13 for cloudy-sky conditions.

409

410

411



412

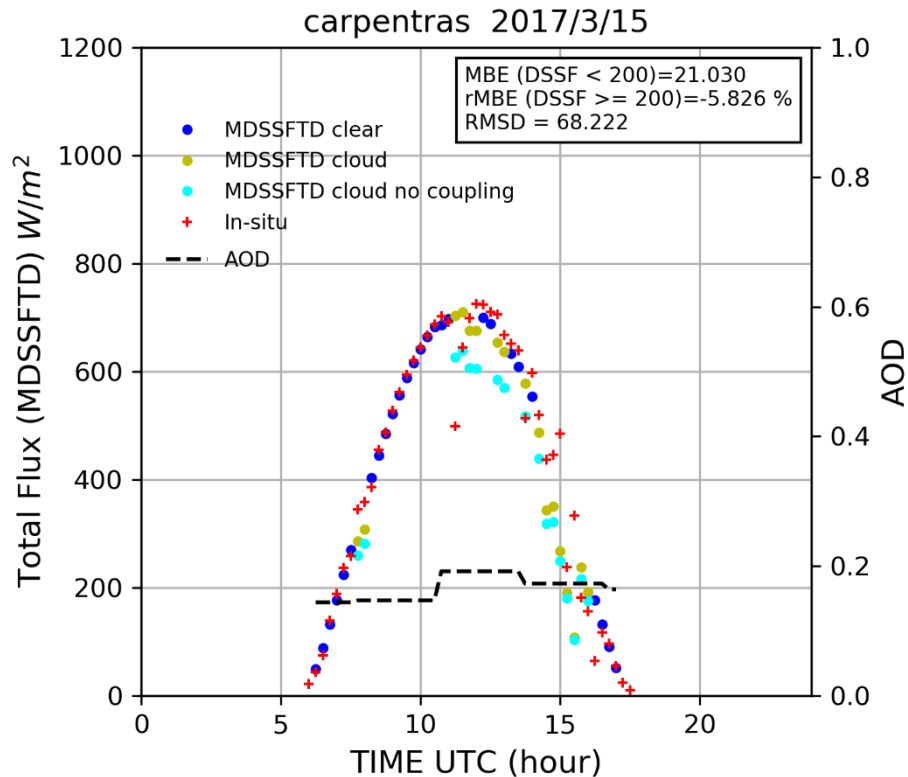
**Figure 15** Same than Figure 13 for all-sky (clear and cloudy) conditions.

413

### 3.5. Impact of the activation of the cloud-aerosol coupling

414  
415  
416  
417  
418  
419  
420

The method for DSSF retrieval is using a simple radiative transfer model that takes into account the radiative coupling between aerosols and clouds as described in the companion paper [40] (see fourth term of Eq. 24). Figure 16 gives an example of this cloud-aerosol coupling for a selected day in Carpentras. We clearly observe a better agreement with the *in-situ* measurements around noon in the case of the activation of the cloud-aerosol radiative coupling (yellow dots compared to light blue dots). Even if the AOD is not large (i.e. 0.2), the impact of the cloud-aerosol coupling remains important. We are here clearly in presence of very thin clouds in the high atmosphere.

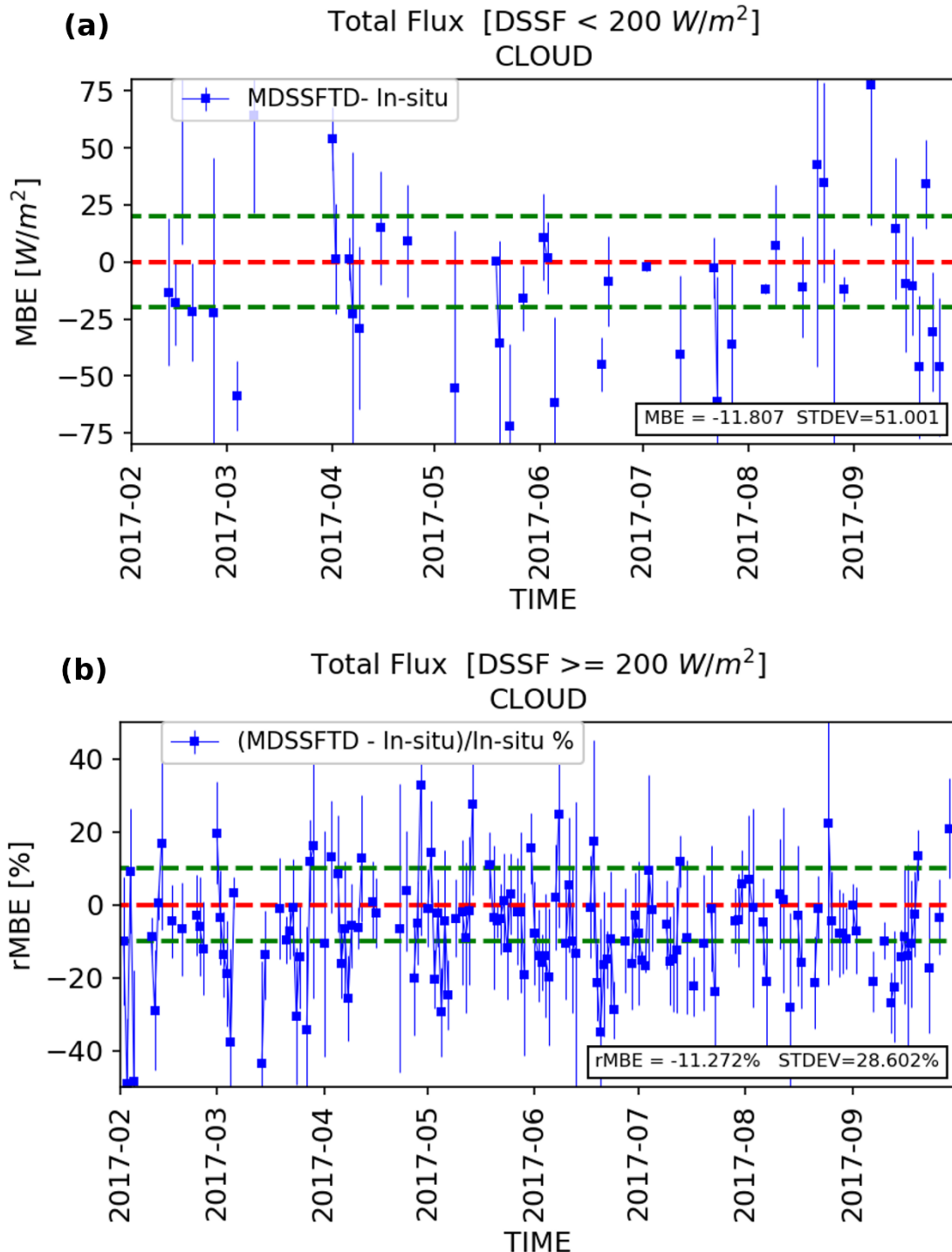


421      **Figure 16** Same diurnal variation than in Figure 5 for Carpentras. Light-blue dots show the  
 422      estimations of total MDSSFTD with 'no coupling' (i.e., no activation of the cloud-aerosol coupling) in  
 423      cloudy conditions. Yellow dots show same LSA-207 DSSF retrievals in cloudy conditions than in  
 424      Figure 5. Black dashed line represents the AOD (CAMS). Statistics in the top right corner are those of  
 425      the MDSSFTD product (with activation of the cloud-aerosol coupling).

426      Figure 11 showed the performances of the DSSF estimated by the MDSSFTD algorithm, which  
 427      considers the influence of the cloud-aerosol coupling under cloudy-sky conditions. MDSSFTD  
 428      satellite estimates are very close to the *in-situ* measurements (MBE=-6.618, rMBE=-2.782%). Figure 17  
 429      now shows the same comparison by using the same code after disabling the coupling between cloud  
 430      and aerosols (by simply removing the fourth term of Eq. 24 in [40]. We clearly observe a large  
 431      degradation of the performances of the algorithm in this case (MBE=-11.807 Wm<sup>-2</sup>, rMBE=-11.272%).  
 432      The presence of aerosols makes the atmospheric transmittance decrease, and in turn the DSSF  
 433      becomes lower. However, this atmospheric transmittance decreasing is too large in cloudy conditions.  
 434      This sensitivity test illustrates the importance of the indirect radiative impacts of clouds on aerosol  
 435      radiative forcing. In our study, the activation of the coupling improves the performances of about 8%.  
 436      Clouds induce an increase of the atmospheric transmittance by reflecting, back to the surface, part of  
 437      the radiation scattered by aerosols. This radiative cloud-aerosol coupling is included in the LSA-207  
 438      product.

439

440

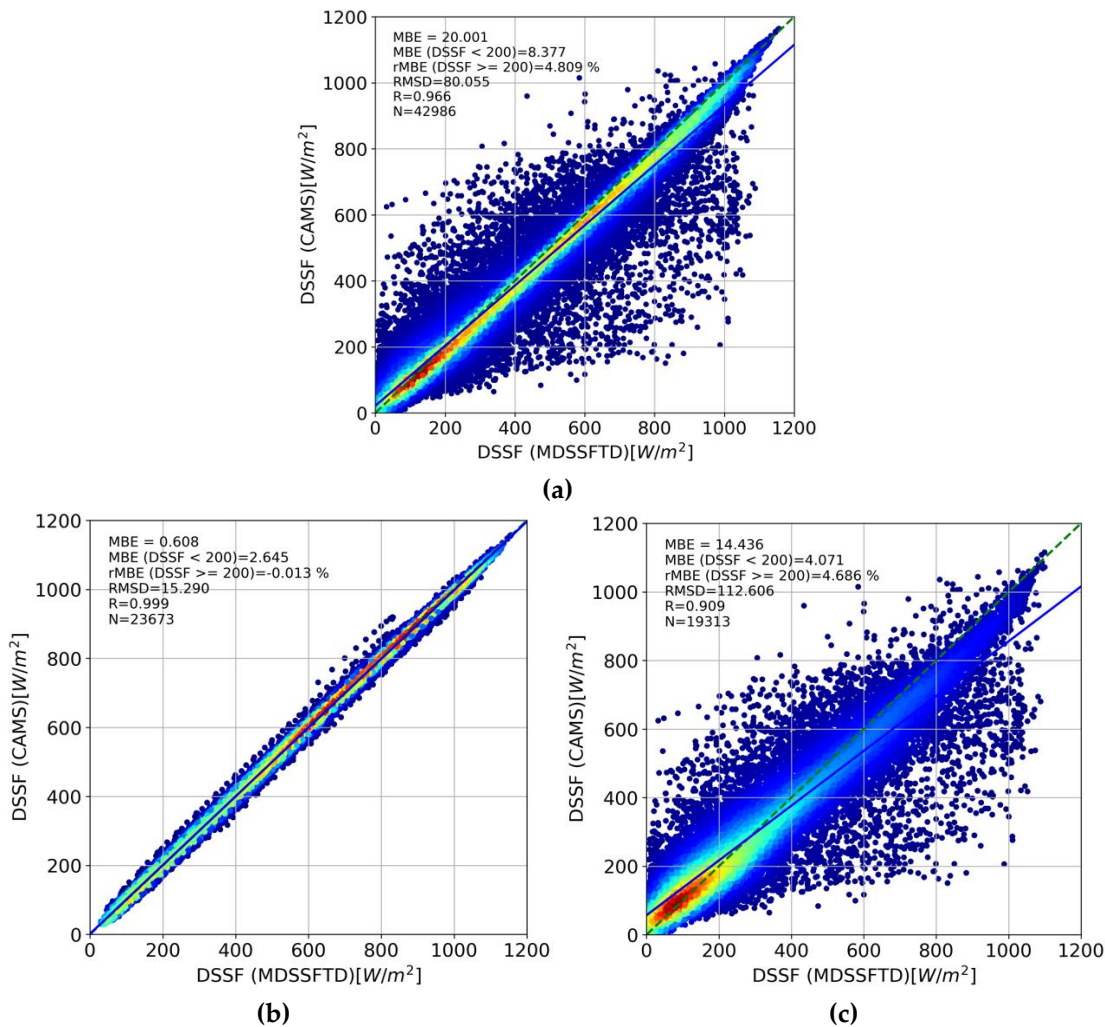


441        **Figure 17** Same than Figure 11 for cloudy-sky conditions but inactivating the coupling between cloud  
 442        and aerosol.

443        *3.6. Comparison to CAMS radiation product*

444        The retrievals from MDSSFTD are compared against the counterpart estimates from the  
 445        CAMS radiation product. Figure 18(a) shows the good agreement between the two products for  
 446        all-sky conditions, with a correlation of 0.966. Figures 18(b) and 18(c) take a further look to the  
 447        comparison by exploring the clear sky and cloudy sky retrievals separately. The clear sky  
 448        comparison gives a high agreement between the two products, which are using CAMS aerosol  
 449        data as input. The comparison for cloudy sky also shows a good agreement (correlation of 0.909)

450 despite the differences of the retrieval methods for cloudy sky conditions. The higher dispersion  
 451 is justified by the increased difficulty of the retrieval for cloudy skies.



452  
 453  
 454  
 455  
 456  
 457  
**Figure 18** Density scatter plots for the comparison between MDSSFTD and CAMS radiation product  
 for (a) all-sky, (b) clear sky, and (c) cloudy sky conditions.

#### 458 4. Conclusions

459 This paper presents the results of the comparison of the LSA-207 MDSSFTD product outputs,  
 460 namely the total DSSF and diffuse fraction (fd) components, against the *in-situ* measurements  
 461 acquired at four BSRN stations over a seven-month period. The validation is performed on  
 462 instantaneous satellite retrievals with MSG/SEVIRI (i.e. acquired every 15 minutes).

463 The results show that the satellite estimates of DSSF and fd meet the requirements for all-sky  
 464 (clear and cloudy) conditions. For DSSF, the requirements are  $20\text{Wm}^{-2}$  for  $\text{DSSF} < 200\text{Wm}^{-2}$  and 10%  
 465 for  $\text{DSSF} \geq 200\text{Wm}^{-2}$ . The MBE and rMBE compared to the ground measurements are  $3.618\text{Wm}^{-2}$  and  
 466 0.252%, respectively. For fd, the requirements are 0.1 for  $\text{fd} < 0.5$  and 20% for  $\text{fd} \geq 0.5$ . The MBE and  
 467 rMBE compared to the ground measurements are -0.044 and -17.699%, respectively.

468 A more detailed analysis of the product performances was also performed separately for clear  
 469 and cloudy sky conditions. For DSSF in clear-sky conditions, the MBE and rMBE compared to the  
 470 ground measurements are  $8.637\text{Wm}^{-2}$  and 0.776%, respectively. For fd, the MBE and rMBE compared  
 471 to the ground measurements are 0.062 and -22.197%, respectively. Thus, the two products outputs  
 472 also meet the target requirements if only clear-sky conditions are selected and if we do not consider  
 473  $\text{fd} \geq 0.5$  case (which is not statistically representative). For DSSF in cloudy-sky conditions, the MBE  
 474 and rMBE compared to the ground measurements are  $-6.618\text{Wm}^{-2}$  and 2.782%, respectively. For fd,  
 475 the MBE and rMBE compared to the ground measurements are 0.027 and -15.796%, respectively. Thus,

476 the product meets the target requirements for all conditions with only a few exceptions. The major  
477 limitations of the retrieval approach described in the companion article [40] are not an obstacle for  
478 meeting the required quality. It is noted that the requirements for the product MDSSFTD are defined  
479 for the all-sky conditions only.

480 In an earlier study by [42], it was shown that the use of MACC-II (now CAMS) AOD forecasts  
481 as input to the MDSSFTD clear sky method instead of reanalyses significantly decreased the quality  
482 of the DSSF products under clear sky conditions. For the last years, the quality of the CAMS AOD  
483 forecasts currently available could have improved, which makes the high sensitivity of the MDSSFTD  
484 diffuse estimation to the quality of AOD forecasts not to be a limitation anymore. Finally, we show  
485 that this AOD information is of primary importance for the estimation of the atmospheric  
486 transmittance either in clear or in cloudy conditions. In cloudy-sky conditions, the modelling of the  
487 cloud-aerosol radiative coupling allows to reduce the overall bias by around 8%.

488 **Acknowledgments:** The work presented in this article has been carried out as part of the CDOP3 activities  
489 related to the exploitation of the MSG/SEVIRI satellite mission in the framework of the EUMETSAT Satellite  
490 Application Facility on Land Surface Analysis (LSA-SAF; <http://lsa-saf.eumetsat.int>).

## 491 References

492 [1] Mateos, D., Antón, M., Valenzuela, A., Cazorla, A., Olmo, F. J., & Alados-Arboledas, L. (2013). Short-wave  
493 radiative forcing at the surface for cloudy systems at a midlatitude site. *Tellus B: Chemical and Physical  
494 Meteorology*, 65(1), 21069.

495 [2] Van Tricht, K., Lhermitte, S., Lenaerts, J.T.M., Gorodetskaya, I.V., L'Ecuyer, T.S., Noël, B., van den Broeke,  
496 M.R., Turner, D.D., van Lipzig, N.P.M., 2016. Clouds enhance Greenland ice sheet meltwater runoff. *Nat.  
497 Commun.* 7, 10266.

498 [3] Mercado, L. M., Bellouin, N., Sitch, S., Boucher, O., Huntingford, C., Wild, M., & Cox, P. M. (2009). Impact of  
499 changes in diffuse radiation on the global land carbon sink. *Nature*, 458(7241), 1014.

500 [4] Carrer, D., Roujean, J. L., Lafont, S., Calvet, J. C., Boone, A., Decharme, B., ... & Gastellu-Etchegorry, J. P.  
501 (2013). A canopy radiative transfer scheme with explicit FAPAR for the interactive vegetation model ISBA-A-gs:  
502 Impact on carbon fluxes. *Journal of Geophysical Research: Biogeosciences*, 118(2), 888-903.

503 [5] O'Sullivan, M. et al. Small global effect on terrestrial net primary production due to increased fossil fuel  
504 aerosol emissions from East Asia since the turn of the century. *Geophys. Res. Lett.* 43, 8060–8067 (2016).

505 [6] Yoshida, S., Ueno, S., Kataoka, N., Takakura, H., & Minemoto, T. (2013). Estimation of global tilted irradiance  
506 and output energy using meteorological data and performance of photovoltaic modules. *Solar Energy*, 93, 90-99.

507 [7] Betts, A. K., S.-Y. Hong, and H.-L. Pan, 1996: Comparison of NCEP–NCAR reanalysis with 1987 FIFE data.  
508 *Mon. Wea. Rev.*, 124, 1480–1498.

509 [8] Brotzge, J. A., 2004: A two-year comparison of the surface water and energy budgets between two OASIS sites  
510 and NCEP–NCAR reanalysis data. *J. Hydrometeor.*, 5, 311–326.

511 [9] Berbery, E. H., K. E. Mitchell, S. Benjamin, T. Smirnova, H. Ritchie, R. Hogue, and E. Radeva, 1999: Assessment  
512 of land-surface energy budgets from regional and global models. *J. Geophys. Res.*, **104**, 19 329–19 348.

513 [10] Schroeder TA, Hamber R, Copps NC and Liang S (2009) Validation of solar radiation surfaces from MODIS  
514 and reanalysis data over topographically complex terrain. *J. App. Meteor. Climat.* **48**, 2441-2458

515 [11] Babst, F., R. W. Mueller, and R. Hollman, 2008: Verification of NCEP reanalysis shortwave radiation with  
516 mesoscale remote sensing data. *IEEE Trans. Geosci. Remote Sens.*, **5**, 34–37.

517 [12] Urraca, R., Huld, T., Gracia-Amillo, A., Martinez-de-Pison, F. J., Kaspar, F., & Sanz-Garcia, A.: Evaluation  
518 of global horizontal irradiance estimates from ERA5 and COSMO-REA6 reanalyses using ground and satellite-  
519 based data, *Solar Energy*, **164**, 339-354, 2018.

520 [13] Bishop, J. K. B., and Rossow, W. B., 1991. Spatial and temporal variability of global surface solar  
521 irradiance. *Journal of Geophysical Research*, **96**, 16389 – 16858.

522 [14] Darnell, W., Staylor, W., Gupta, S., and Denn, F., 1988. Estimation of surface insolation using sun-  
523 synchronous satellite data. *Journal of Climate*, **1**, 820 – 835.

524 [15] Dedieu, G. P., Deschamps, P., and Kerr, Y., 1987. Satellite estimation of solar irradiance at the surface of the  
525 earth and of surface albedo using a physical model applied to METEOSAT data. *Journal of Climate and Applied  
526 Meteorology*, **26**, 79 –87.

527 [16] Gautier C., Diak G., Masse S., 1980, A simple physical model to estimate incident solar radiation at the  
528 surface from GOES satellite data, *J. Climate Appl. Meteor.*, **19**, 1005-1012.

529 [17] Cano, D., Monget, J. M., Albuisson, M., Guillard, H., Regas, N., Wald, L., 1986: A method for the  
530 determination of the global solar radiation from meteorological satellite data. *Solar Energy*, **37**, 31±39.

531 [18] Gautier, C., & Landsfeld, M. (1997). Surface solar radiation flux and cloud radiative forcing for the  
532 Atmospheric Radiation Measurement (ARM) Southern Great Plains (SGP): A satellite, surface observations, and  
533 radiative transfer model study. *Journal of the atmospheric sciences*, **54**(10), 1289-1307.

534 [19] Li, Z., and Leighton, H. G. (1993). Global climatologies of the solar radiation budgets at the surface and in  
535 the atmosphere from 5 years of ERBE data. *Journal of Geophysical Research*, **98**, 4919 – 4930.

536 [20] Masuda, K., Leighton, H. G., & Li, Z. (1995). A new parameterization for the determination of solar flux  
537 absorbed at the surface from satellite measurements. *Journal of Climate*, **8**(6), 1615-1629.

538 [21] Hammer, A., Heinemann, D., Lorenz, E., & Lućkehe, B. (1999). Short- term forecasting of solar radiation  
539 based on image analysis of meteosat data. *Proc. EUMETSAT meteorological satellite data users conference* (pp.  
540 331-337).

541 [22] Möser, W., and E. Raschke, 1984: Incident solar radiation over Europe from METEOSAT data. *J. Climate*  
542 *Appl. Meteor.*, **23**, 166–170.

543 [23] Pinker, R., and Ewing, J. (1985). Modeling surface solar radiation: model formulation and validation. *Journal*  
544 *of Climate and Applied Meteorology*, **24**, 389 – 401.

545 [24] Pinker, R., and Laszlo, I. (1992). Modeling surface solar irradiance for satellite applications on a global scale.  
546 *Journal of Applied Meteorology*, **31**, 194 – 211.

547 [25] Tarpley, J. (1979). Estimating incident solar radiation at the surface from geostationary satellite data. *Journal*  
548 *of Climate and Applied Meteorology*, **18**, 1172 –181.

549 [26] Whitlock, C. H., Charlock, T. P., Staylor, W. F., Pinker, R. T., Laszlo, I., Ohmura, A., Gilgen, H., Konzelman,  
550 T., DiPasquale, R. C., Moats, C. D., LeCroy, S. R., and Ritchey, N. A. (1995). First global WCRP shortwave surface  
551 radiation budget dataset. *Bulletin of the American Meteorological Society*, **76**, 905 – 922.

552 [27] Romano, F.; Cimini, D.; Cersosimo, A.; Di Paola, F.; Gallucci, D.; Gentile, S.; Geraldi, E.; Larosa, S.; T. Nilo,  
553 S.; Ricciardelli, E.; Ripepi, E.; Viggiano, M. Improvement in Surface Solar Irradiance Estimation Using  
554 HRV/MSG Data. *Remote Sens.* **2018**, *10*, 1288.

555 [28] Gallucci, D.; Romano, F.; Cersosimo, A.; Cimini, D.; Di Paola, F.; Gentile, S.; Geraldi, E.; Larosa, S.; Nilo, S.T.;  
556 Ricciardelli, E.; Viggiano, M. Nowcasting Surface Solar Irradiance with AMESIS via Motion Vector Fields of  
557 MSG-SEVIRI Data. *Remote Sens.* **2018**, *10*, 845.

558 [29] Ineichen, P. High Turbidity Solis Clear Sky Model: Development and Validation. *Remote Sens.* **2018**, *10*,  
559 435.

560 [30] Trigo, I. F., C. C. DaCamara, P. Viterbo, J.-L. Roujean, F. Olesen, C. Barroso, F. Camacho-de-Coca, D.  
561 Carrer, S. C. Freitas, J. García-Haro, B. Geiger, F. Gellens-Meulenberghs, N. Ghilain, J. Meliá, L. Pessanha, N.  
562 Siljamo, A Arboleda (2011), The Satellite Application Facility on Land Surface Analysis, *Int. J. Remote Sens.*, ,  
563 32, 2725-2744.

564 [31] Ineichen, P., Barroso, C. S., Geiger, B., Hollmann, R., Marsouin, A., and Mueller, R.: Satellite Application  
565 Facilities irradiance products: hourly time step comparison and validation over Europe, *Int. J. Remote Sens.*, **30**,  
566 doi:0.1080/01431160802680560, 2009.

567 [32] Roerink, G. J., Bojanowski, J., de Wit, A. J. W., Eerens, H., Supit, I., Leo, O., and Boogaard, H. L. (2012)  
568 Evaluation of MSG-derived global radiation estimates for application in a regional crop model. *Agricultural*  
569 *and Forest Meteorology*, **160**:36–47.

570 [33] Moreno, A. & Gilabert, M.A. & Camacho, F. & Martínez, B., 2013. "Validation of daily global solar  
571 irradiation images from MSG over Spain," *Renewable Energy*, Elsevier, vol. 60(C), pages 332-342.

572

573 [34] Bevan, S. L., North, P. R. J., Los, S. O., and Grey, W. M. F.: A global dataset of atmospheric aerosol optical depth and  
574 surface reflectance from AATSR, *Remote Sens. Environ.*, **116**, 199–210, 2012.

575 [35] Jayaraman, A., Lubin, D., Ramachandran, S., Ramanathan, V., Woodbridge, E., Collins, W.D., Zalpuri, K.S.,  
576 1998. Direct observations of aerosol radiative forcing over the tropical Indian Ocean during the January–February  
577 1996 pre-INDOEX cruise. *J. Geophys. Res. Atmospheres* **103**, 13827–13836.

578 [36] Satheesh, S.K., Ramanathan, V., 2000. Large differences in tropical aerosol forcing at the top of the  
579 atmosphere and Earth's surface. *Nature* **405**, 60–63. doi:10.1038/35011039

580 [37] Cherian, R., Quaas, J., Salzmann, M., Wild, M., 2014. Pollution trends over Europe constrain global aerosol  
581 forcing as simulated by climate models. *Geophys. Res. Lett.* **41**, 2176–2181. doi:10.1002/2013GL058715

582 [38] Dramé, M. S., Ceamanos, X., Roujean, J. L., Boone, A., Lafore, J. P., Carrer, D., & Geoffroy, O. (2015). On the  
583 Importance of Aerosol Composition for Estimating Incoming Solar Radiation: Focus on the Western African  
584 Stations of Dakar and Niamey during the Dry Season. *Atmosphere*, **6**(11), 1608–1632.

585 [39] Kosmopoulos, P.G., Kazadzis, S., Taylor, M., Athanasopoulou, E., Speyer, O., Raptis, P.I., Marinou, E.,  
586 Proestakis, E., Solomos, S., Gerasopoulos, E., Amiridis, V., Bais, A. and Kontoes, C. (2017). Dust impact on  
587 surface solar irradiance assessed with model simulations, satellite observations and ground-based  
588 measurements. *Atmos. Meas. Tech.* **10**: 2435–2453.

589 [40] Carrer, D., Ceamanos., X., Moparthy, M., Vincent, C., Coehlo, S., Trigo, I., 2019. Satellite retrieval of  
590 downwelling shortwave surface flux and diffuse fraction under all sky conditions in the framework of the LSA  
591 SAF program (part 1: methodology). Submitted.

592 [41] Ceamanos, X., Carrer, D., Roujean, J.-L., An efficient approach to estimate the transmittance and reflectance  
593 of a mixture of aerosol components, *Atmospheric Research*, Vol. 137, Feb. 2014a, pp. 125–135

594 [42] Ceamanos, X., Carrer, D., Roujean, J.-L., 2014b. Improved retrieval of direct and diffuse downwelling surface  
595 shortwave flux in cloudless atmosphere using dynamic estimates of aerosol content and type: application to the  
596 LSA-SAF project. *Atmospheric Chem. Phys.* **14**, 8209–8232. doi:10.5194/acp-14-8209-2014

597 [43] Riihelä, A.; Kallio, V.; Devraj, S.; Sharma, A.; Lindfors, A. Validation of the Sarah-e satellite-based surface

598 [44] Riihelä, A.; Carlund, T.; Trentmann, J.; Müller, R.; Lindfors, A.V. Validation of CM SAF Surface Solar  
599 Radiation Datasets over Finland and Sweden. *Remote Sens.* **2015**, *7*, 6663–6682.

600 [45] Geiger, B., Meurey, C., Lajas, D., Franchistéguy, L., Carrer, D., & Roujean, J. L. (2008). Near real-time  
601 provision of downwelling shortwave radiation estimates derived from satellite observations. *Meteorological  
602 Applications*, **15**(3), 411–420.

603 [46] Carrer, D., Lafont, S., Roujean, J.-L., Calvet, J.-C., Meurey, C., Le Moigne, P., and Trigo, I. : Incoming solar  
604 and infrared radiation derived from METEOSAT: impact on the modelled land water and energy budget over  
605 France, *J. Hydrometeor.*, **13**, 504–520, 2012.

606 [47] McArthur, L. J. B. "Baseline Surface Radiation Network (BSRN)-Operation Manual Version 2.1." (2005).

607 [48] Vuilleumier, L., Hauser, M., Félix, C., Vignola, F., Blanc, P., Kazantzidis, A., & Calpini, B. (2014). Accuracy  
608 of ground surface broadband shortwave radiation monitoring. *Journal of geophysical research: atmospheres*,  
609 **119**(24), 13-838.

610 [49] García, R. D., Cuevas, E., Ramos, R., Cachorro, V. E., Redondas, A., & Moreno-Ruiz, J. A. (2019). Description  
611 of the Baseline Surface Radiation Network (BSRN) station at the Izaña Observatory (2009–2017): measurements  
612 and quality control/assurance procedures. *Geoscientific Instrumentation, Methods and Data Systems*, **8**(1), 77–  
613 96.

614 [50] Qu, Z., Oumbe, A., Blanc, P., Espinar, B., Gesell, G., Gschwind, B., ... & Wald, L. (2017). Fast radiative  
615 transfer parameterisation for assessing the surface solar irradiance: The Heliosat-4 method. *Meteorologische  
616 Zeitschrift*, **26**(1), 33-57.

617 [51] Lefèvre, M., Oumbe, A., Blanc, P., Espinar, B., Gschwind, B., Qu, Z., ... & Benedetti, A. (2013). McClear: a  
618 new model estimating downwelling solar radiation at ground level in clear-sky conditions. *Atmospheric  
619 Measurement Techniques*, **6**, 2403-2418.

620 [52] Gschwind, B., Wald, L., Blanc, P., Lefèvre, M., Schroedter-Homscheidt, M., & Arola, A. (2019). Improving  
621 the McClear model estimating the downwelling solar radiation at ground level in cloud-free conditions—  
622 McClear-v3. *Meteorologische Zeitschrift*.

623 [53] Mayer, B., & Kylling, A. (2005). The libRadtran software package for radiative transfer calculations—  
624 description and examples of use. *Atmospheric Chemistry and Physics*, **5**(7), 1855-1877.

625 [54] Blanc, P., B. Gschwind, M. Lefèvre, L. Wald, 2014: Twelve monthly maps of ground albedo parameters  
626 derived from MODIS data sets. In *Proceedings of IGARSS 2014*, held 13-18 July 2014, Quebec, Canada,  
627 USBKey, pp. 3270-3272.

628 [55] Schaaf, C. B., Gao, F., Strahler, A. H., Lucht, W., Li, X., Tsang, T., ... & Lewis, P. (2002). First operational  
629 BRDF, albedo nadir reflectance products from MODIS. *Remote sensing of Environment*, **83**(1-2), 135-148.

630 [56] Kriebel, K. T., Saunders, R. W., & Gesell, G. (1989). Optical properties of clouds derived from fully cloudy  
631 AVHRR pixels. *Beiträge zur Physik der Atmosphäre*, **62**, 165-171.

632 [57] Kriebel, K. T., Gesell, G., Ka“ Stner, M., & Mannstein, H. (2003). The cloud analysis tool APOLLO:  
633 improvements and validations. *International journal of remote sensing*, 24(12), 2389-2408.

634 [58] Hakuba MZ, Folini D, Sanchez-Lorenzo A, Wild M (2013) Spatial representativeness of ground-based solar  
635 radiation measurements. *J Geophys Res* 118:8585–8597.

636 [59] Erbs, D.G., Klein, S.A., Duffie, J.A., 1982. Estimation of the diffuse radiation fraction for hourly, daily and  
637 monthly-average global radiation. *Sol. Energy* 28, 293–302. doi:10.1016/0038-092X(82)90302-4

638 [60] Reindl DT, Beckman WA, Duffie JA. Diffuse fraction correlations. *Solar Energy* 1990;45:1–7.

639 [61] Orgill JF, Hollands KGT. Correlation equation for hourly diffuse radiation on a horizontal surface. *Solar  
640 Energy*, 1977;19:357–9.

641 [62] Louche A, Notton G, Poggi P, Simonnot G. Correlations for direct normal and global horizontal irradiation  
642 on French Mediterranean site. *Solar Energy* 1991;46:261–6.